

Testing Gravity using Cosmic Voids

Yan-Chuan Cai^{1*}, Nelson Padilla^{2,3†}, Baojiu Li^{1,‡}

¹*Institute for Computational Cosmology, Department of Physics, University of Durham, South Road, Durham DH1 3LE, UK*

²*Instituto de Astrofísica, Pontificia Universidad Católica, Av. Vicuña Mackenna 4860, Santiago, Chile.*

³*Centro de Astro-Ingeniería, Pontificia Universidad Católica, Av. Vicuña Mackenna 4860, Santiago, Chile.*

1 October 2018

ABSTRACT

We explore voids in dark matter and halo fields from simulations of Λ CDM and Hu-Sawicky $f(R)$ models. In $f(R)$ gravity, dark matter void abundances are greater than that of general relativity (GR). However, when using haloes to identify voids, the differences of void abundances become much smaller. In contrast to the naive expectation, the abundance of large voids found using haloes in $f(R)$ gravity is lower than in GR. The more efficient halo formation in underdense regions makes $f(R)$ voids less empty. This counter intuitive result suggests that voids are not necessarily emptier in $f(R)$ if one looks at galaxies or groups in voids. However, while the halo number density profiles of voids are not distinguishable from GR, the same $f(R)$ voids are indeed more empty of dark matter. This can in principle be observed by weak gravitational lensing of voids, for which the combination of a spec- z and a photo- z survey over the same sky is necessary. For a volume of 1 (Gpc/h)³, $f(R)$ model parameter amplitudes of $|f_{R0}| = 10^{-5}$ and $|f_{R0}| = 10^{-4}$ can be told apart from GR using the lensing tangential shear signal around voids by 4 and 8σ . We find that line-of-sight projections of large-scale structure is the main systematics that limits the significance of this signal, limiting the constraining power for $|f_{R0}| = 10^{-6}$. We expect that this limitation can be overcome with larger volumes. The outflow of mass from void centers are 5%, 15% and 35% more rapidly in $f(R)$ for $|f_{R0}| = 10^{-6}$, $|f_{R0}| = 10^{-5}$ and $|f_{R0}| = 10^{-4}$. The velocity dispersions are greater than GR by similar amounts. The absolute differences are greater for large voids. Model differences in velocity profiles imply potential powerful constraints of the model in phase space and in redshift space.

Key words: gravitational lensing: weak – methods: statistical – gravitation – large-scale structure of Universe

1 INTRODUCTION

Cosmic voids as cosmological probes have been explored in many aspects. For examples, the Alcock-Paczynski test using stacking of voids has been demonstrated to be a powerful probe of distance distortions between the line-of-sight and transverse directions (Lavaux & Wandelt 2012; Sutter et al. 2014); stacking of voids for the cosmic microwave background has been used as an alternative to the cross-correlation method to detect the integrated Sachs Wolfe effect (Cai et al. 2014, 2013; Granett et al. 2008; Hotchkiss et al. 2014; Ilić et al. 2013; Planck Collaboration et al. 2013); the weak gravitational lensing effect of voids, as an analogue to that of haloes, has been shown to be capable of measuring the matter density profiles of voids (Clampitt & Jain 2014; Melchior et al. 2014); void ellipticity has been shown to be sensitive to the dark energy equation of state (Bos et al. 2012); void properties have been stud-

ied in dynamical dark energy (Bos et al. 2012), coupled dark energy (Li 2011; Sutter et al. 2014) and modified gravity (Li et al. 2012) models using N-body simulations.

The basic properties of voids – their abundances and density profiles – can be powerful in constraining theories of cosmology and gravity, but there are still gaps between observations and theoretical predictions for these two properties. The reasons are partly related to the technical details of how voids are defined: 1) given the same simulation, different void-finding algorithms do not usually find the same voids (Colberg et al. 2008); 2) voids defined using tracers (galaxies or haloes) are expected to be different from voids defined using the dark matter field. Nevertheless, studies of void profiles have made encouraging progress in the last decades. Applying a spherical under-density algorithm to find voids in N-body simulations, Colberg et al. (2005) have found that void profiles are self-similar within the effective void radius they defined, (but see Ricciardelli et al. 2014). Using ZOBOV (Neyrinck et al. 2005), Hamaus et al. (2014) have found that dark matter void profiles within a wide range of radii can be similar if rescaled using two free parameters. Using mocks and real LRG galaxies from SDSS,

* E-mail: y.c.cai@durham.ac.uk

† npadilla@astro.puc.cl

‡ E-mail: baojiu.li@durham.ac.uk

Nadathur et al. (2014) found an even simpler rescaling relationship among voids of different sizes, using only one parameter.

It is perhaps more challenging to use void abundance to constrain cosmology. Excursion set theory offers predictions of the void abundance but the agreement with N-body simulations is never as great as in the case of haloes (Sheth & van de Weygaert 2004; Colberg et al. 2005; Paranjape et al. 2011; Achitouv et al. 2013). A recent attempt to compare void abundance between simulations and excursion set theory has found that they may agree at $\sim 16\%$ at $z = 0$ if dark matter is used to define voids in simulations (Jennings et al. 2013), but the agreement is much worse if haloes are used instead. It would be even harder to compare theoretical predictions with observed void abundances from galaxy surveys due to the systematics introduced by survey geometry and masks. One possible way to overcome this is to apply the same algorithm to simulations and observations, that makes comparisons of void properties with simulations meaningful.

In this work, we will focus on the potential of using the above two basic properties of voids to constrain modified gravity. Scalar-field models of modified gravity could drive the late-time accelerated expansion of the Universe without explicitly invoking a cosmological constant. Although such theories often introduce extra long-range forces (known as fifth forces) mediated by the scalar fields, they can still in principle pass local tests of gravity via certain screening mechanisms, such as Vainshtein (Vainshtein 1972) or chameleon (Khouri & Weltman 2004) mechanisms. More explicitly, the success of those models largely relies on the screening mechanism to suppress the fifth force in over-dense regions, where most of current astronomical observables come from. It is therefore inbuilt in these models that their differences from general relativity (GR) are minimal in high density environments like dark matter haloes, galaxies and the local Solar system. Nevertheless, in these models, the growth of structure is altered to some extent due to the coupling of scalar fields with matter, though the ensemble average of the growth at large scales might still be the same as in Λ CDM (Jennings et al. 2012; Li et al. 2013). For example, in the $f(R)$ model (Hu & Sawicki 2007), which is mathematically equivalent to the coupled scalar field model mentioned above, the difference from Λ CDM in terms of the halo mass function and matter power spectrum are not yet in obvious contradiction with observational data (see below). It is therefore interesting and necessary to explore alternative probes that are sensitive to the environment-dependent nature of these models.

Voids in modified gravity have previously been studied by Li et al. (2012) using N-body simulations, and by Martino & Sheth (2009); Clampitt et al. (2013); Lam et al. (2014) using analytical methods. For chameleon-type coupled scalar field models, the fifth force is found to counter the standard Newtonian gravity in underdensities (Clampitt et al. 2013). The repulsive force drives underdensities to expand faster and grow larger, hence also changing the distribution and abundances of voids. This naturally implies that the two basic properties of voids, their density profiles and abundances, can be promising tools to probe and constrain modified gravity.

In this work, we use a set of N-body simulations of the $f(R)$ model to study of properties of voids in detail, focusing on prospective observables to distinguish the $f(R)$ model from GR using voids. In section 2, the basics of the $f(R)$ models and the N-body simulations are introduced. Section 3 summarise our void-finding algorithm. We present the main results of comparing void properties, and discuss the observational implications in Section 4 and Section 5.

2 THE $f(R)$ GRAVITY MODEL AND ITS SIMULATIONS

In this section we briefly introduce the theory and simulations of $f(R)$ gravity, to make this paper self contained.

2.1 The $f(R)$ gravity model

The $f(R)$ gravity model (Carroll et al. 2005) generalises GR by simply replacing the Ricci scalar R in the standard Einstein-Hilbert action by an algebraic function $f(R)$ (see e.g. Sotiriou & Faraoni 2010; De Felice & Tsujikawa 2010, for some recent reviews):

$$S = \int d^4x \sqrt{-g} \left\{ \frac{M_{\text{Pl}}^2}{2} [R + f(R)] + \mathcal{L}_m(\psi_i) \right\}, \quad (1)$$

where M_{Pl} is the reduced Planck mass, and is related to Newton's constant G by $M_{\text{Pl}}^{-2} = 8\pi G$, g is the determinant of the metric tensor $g_{\mu\nu}$ and $\mathcal{L}_m(\psi_i)$ the Lagrangian density for matter, in which ψ_i symbolically denotes the matter field for the i -th species, i running over photons, neutrinos, baryons and cold dark matter. By fixing the functional form of $f(R)$, one fully specifies a $f(R)$ gravity model.

Variation of the action Eq. (1) with respect to the metric tensor $g_{\mu\nu}$ leads to the modified Einstein equation

$$G_{\mu\nu} + f_R R_{\mu\nu} - g_{\mu\nu} \left[\frac{1}{2} f - \square f_R \right] - \nabla_\mu \nabla_\nu f_R = 8\pi G T_{\mu\nu}^m, \quad (2)$$

where $G_{\mu\nu} \equiv R_{\mu\nu} - \frac{1}{2} g_{\mu\nu} R$ is the Einstein tensor, $f_R \equiv df/dR$, ∇_μ is the covariant derivative compatible to $g_{\mu\nu}$, $\square \equiv \nabla^\alpha \nabla_\alpha$ and $T_{\mu\nu}^m$ the energy momentum tensor for matter fields. Eq. (2) is a differential equation containing up to fourth-order derivatives of the metric tensor, because R itself contains second derivatives of $g_{\mu\nu}$. It is often helpful to consider it as the standard second-order Einstein equation for general relativity, which is additionally sourced by a new, scalar, dynamical degree of freedom – the so-called scalaron field f_R . The equation of motion for f_R can be derived by simply taking the trace of Eq. (2), as

$$\square f_R = \frac{1}{3} (R - f_R R + 2f + 8\pi G \rho_m), \quad (3)$$

where ρ_m is the matter density. Note that in writing this equation we have assumed no massive neutrinos. This equation does not assume that radiations (photons and massless neutrinos) are negligible, because both are traceless, but in what follows we do assume this, since we will be considering the late-time cosmology of $f(R)$ gravity.

We consider a universe with no spatial curvature, and thus the background evolution is described by the flat Friedman-Robertson-Walker (FRW) metric. The line element of the real, perturbed, Universe is expressed in the Newtonian gauge as

$$ds^2 = a^2(\eta) \left[(1 + 2\Phi) d\eta^2 - (1 - 2\Psi) dx^i dx_i \right], \quad (4)$$

where η and x^i are the conformal time and comoving coordinates, and $\Phi(\eta, \mathbf{x})$, $\Psi(\eta, \mathbf{x})$ are respectively the Newtonian potential and perturbed spatial curvature, which depend on both time η and space \mathbf{x} ; a is the scale factor of the Universe and $a = 1$ today.

We are interested in the formation of large-scale structures on scales substantially below the horizon. Under this assumption, the time variation of f_R is small for the models to be studied, and thus we shall work with the quasi-static approximation by neglecting the time derivatives of f_R in all field equations. The equation of motion of f_R , Eq. (3), then simplifies to reduces to

$$\bar{\nabla}^2 f_R = -\frac{1}{3} a^2 [R(f_R) - \bar{R} + 8\pi G (\rho_m - \bar{\rho}_m)], \quad (5)$$

in which $\vec{\nabla}$ is the 3-dimensional gradient operator (we use an arrow to distinguish this from the ∇_μ introduced above), and the overbar takes the background averaged value of the quantity under it. Note that R has been expressed as a function of f_R by reverting $f_R(R)$.

Also in the quasi-static approximation, the (modified) Poisson equation, which determines the behaviour of the Newtonian potential Φ , can be written as

$$\vec{\nabla}^2 \Phi = \frac{16\pi G}{3} a^2 (\rho_m - \bar{\rho}_m) + \frac{1}{6} a^2 [R(f_R) - \bar{R}], \quad (6)$$

where, in addition to the time derivatives of f_R , we have also neglected those of Φ . We have used Eq. (5) to eliminate $\vec{\nabla}^2 f_R$ from Eq. (6).

From the above equations, we see that there are two potential cosmological implications of the scalaron field: (i) the background expansion of the Universe can be altered by the new terms in Eq. (2) and (ii) the relationship between the gravitational potential Φ and the matter density perturbation is altered, which can cause changes to the growth of density perturbations.

It is useful to inspect in which conditions is the general relativistic (or Newtonian) limit recovered. Evidently, when $|f_R| \ll 1$, Eq. (5) gives $R \approx -8\pi G \rho_m$ and so Eq. (6) reduces to the normal Poisson equation of general relativity:

$$\vec{\nabla}^2 \Phi = 4\pi G a^2 (\rho_m - \bar{\rho}_m). \quad (7)$$

When $|f_R|$ is large, we instead have $|R - \bar{R}| \ll 8\pi G |\rho_m - \bar{\rho}_m|$ and then Eq. (6) reduces to the normal Poisson equation but with G enhanced by 1/3:

$$\vec{\nabla}^2 \Phi = \frac{16\pi G}{3} a^2 (\rho_m - \bar{\rho}_m). \quad (8)$$

The value 1/3 is the maximum enhancement factor of the strength of gravitational interaction in $f(R)$ models, independent of the specific functional form of $f(R)$. Nevertheless, the choice of $f(R)$ is important because it determines the scalaron dynamics and therefore at what time and scale the enhancement factor switches from 1/3 to 0: scales substantially larger than the Compton wavelength of f_R (which characterises the range of the scalaron-mediated modification to Newtonian gravity) are unaffected and gravity is as predicted by general relativity there; on small scales, however, depending on the dynamical properties of Eq. (5), the 1/3 enhancement could be fully realised – this leads to a scale-dependent modification of gravity and consequently scale-dependent evolution of cosmic structures.

2.2 The chameleon mechanism

The $f(R)$ model would have been ruled out by Solar system gravity tests due to the factor-of-4/3 rescaling to the strength of Newtonian gravity. Nevertheless, it is known that, if the functional form of $f(R)$ is chosen carefully (Brookfield et al. 2006; Navarro & Van Acoleyen 2007; Li & Barrow 2007; Hu & Sawicki 2007; Brax et al. 2008), the model can use the so-called chameleon mechanism (Khoury & Weltman 2004) to suppress the effects of the scalaron field and therefore reduce to standard gravity in regions with deep enough gravitational potentials, such as our Solar system.

The chameleon mechanism can be understood as the following: the modification to the Newtonian gravity is usually considered as an extra, or fifth, force mediated by the scalaron field. Because the scalaron, unlike gravitons of general relativity, has a mass, this extra force has the Yukawa form, which decays exponentially when

the distance r between two test masses increases, as $\propto \exp(-mr)$, in which m is the scalaron mass, defined as

$$m^2 \equiv \frac{d^2 V_{\text{eff}}(f_R)}{df_R^2}, \quad (9)$$

in which V_{eff} is the effective potential for the scalaron (see below), which usually has a minimum which depends on local matter density. In high matter density environments, m is very heavy and the exponential decay causes a strong suppression of the fifth force. In term of the effective potential, this is equivalent to saying that f_R is trapped to the minimum of $V_{\text{eff}}(f_R)$, which itself is restricted to be very close to zero: consequently, $|f_R| \ll 1$ in such environments, and this leads to the GR limit as we have discussed above¹.

As we will see below, V_{eff} is determined by the function form of $f(R)$. Consequently, as mentioned earlier, the latter plays a crucial role of deciding whether the fifth force can be sufficiently suppressed in dense environments. In this paper we will focus on the $f(R)$ model proposed by Hu & Sawicki (2007), which is specified by

$$f(R) = -M^2 \frac{c_1 (-R/M^2)^n}{c_2 (-R/M^2)^n + 1}, \quad (10)$$

where $M^2 \equiv 8\pi G \bar{\rho}_{m0}/3 = H_0^2 \Omega_m$ is a new mass scale, with H being the Hubble expansion rate and Ω_m the present-day fractional energy density of matter. Hereafter, a subscript ₀ always means taking the present-day ($a = 1$) value of a quantity.

At the cosmological background level, the scalaron field f_R always closely follows the minimum of V_{eff} , which itself is related to $f(R)$ (and local matter density - remember the chameleon mechanism depends on this) by

$$V_{\text{eff}}(f_R) \equiv \frac{1}{3} (R - f_R R + 2f + 8\pi G \rho_m). \quad (11)$$

Therefore we find

$$-\bar{R} \approx 8\pi G \bar{\rho}_m - 2\bar{f} \approx 3M^2 \left(a^{-3} + \frac{2c_1}{3c_2} \right), \quad (12)$$

where for the first ‘ \approx ’ we have used $|f_R| \ll 1$, which holds true for the models to be studied in this paper (see below), and for the second we have used the fact that $|\bar{R}| \gg M^2$ throughout the evolution history of our Universe (see the discussion of Eq. (14) below).

To reproduce the background expansion history of the standard Λ CDM paradigm, we set

$$\frac{c_1}{c_2} = 6 \frac{\Omega_\Lambda}{\Omega_m} \quad (13)$$

where $\Omega_\Lambda = 1 - \Omega_m$ is the present-day fractional energy densities of ‘dark energy’ (remember that we have neglected radiations at late times).

By setting $\Omega_\Lambda = 0.76$ and $\Omega_m = 0.24^2$, we find that $|\bar{R}| \approx$

¹ Although it is not technically incorrect to say that the chameleon mechanism works in high-density regions, those regions need to be large enough, e.g., at least comparable to the local Compton wavelength of the scalaron field. Otherwise, the chameleon mechanism does not necessarily work. For this reason, it is more accurate to say that the screening happens in regions with deep Newtonian potential. Nevertheless, in this paper we shall not distinguish between the two.

² These values are currently outdated, but they have been used in the $f(R)$ simulations extensively in the literature, including the ones on which this paper is based. We remark that for the purpose of this study, the exact value of Ω_m is not crucial, as confirmed by some test simulations with different Ω_m .

$41M^2 \gg M^2$ today (and $|\bar{R}|$ is even larger at early times), and this simplifies the expression of the scalaron to

$$f_R \approx -n \frac{c_1}{c_2^2} \left(\frac{M^2}{-R} \right)^{n+1} < 0. \quad (14)$$

Therefore, the two free parameters n and c_1/c_2^2 completely specify this special $f(R)$ model. Moreover, they are related to the value of the scalaron today (f_{R0}) by

$$\frac{c_1}{c_2^2} = -\frac{1}{n} \left[3 \left(1 + 4 \frac{\Omega_\Lambda}{\Omega_m} \right) \right]^{n+1} f_{R0}. \quad (15)$$

In the present paper we will study three $f(R)$ models with $n = 1$ and $|f_{R0}| = 10^{-6}, 10^{-5}, 10^{-4}$, which will be referred to as F6, F5 and F4 respectively. These choices of $|f_{R0}|$ are designed to cover the part of the parameter space which is cosmologically interesting: if $|f_{R0}| > 10^{-4}$ then the $f(R)$ model violates the cluster abundance constraints (Schmidt et al. 2009), and if $|f_{R0}| < 10^{-6}$ then the model is too close to Λ CDM to be distinguishable in cosmology. Lombriser (2014) gives an excellent review on the current cosmological and astrophysical constraints on f_{R0} .

The environmental dependence of the screening means that gravity can behave very differently in different situations. The matter clustering in overdense regions, e.g., dark matter haloes, in $f(R)$ gravity has been studied in great detail, and research shows that the chameleon mechanism can be very efficient in suppressing the fifth force. We will focus on voids, i.e., underdense regions, in this paper, where the chameleon mechanism is expected to work less well and so deviation from standard Newtonian gravity would be stronger.

2.3 The N-body simulations of $f(R)$ gravity

According to Eqs. (5, 6), if the matter density field is known, one can solve the scalaron field f_R from Eq. (5) and plug the solution into the modified Poisson equation, Eq. (6), to compute Φ . When Φ is known, a numerical differentiation will give the total (modified) gravitational force that determines the motions of particles. Such is the basic logic and procedure of $f(R)$ N -body simulations.

The major challenge, then, is to numerically solve the highly nonlinear scalaron equation of motion, Eq. (5), to accurately calculate the gravitational force when the chameleon screening is working. Since there is no analytical force law (such as the r^{-2} -law in Newtonian gravity), it is usually convenient to solve f_R on a mesh (or a suite of meshes) using relaxation methods. This implies that mesh-based N -body codes are most suitable.

N -body simulations of $f(R)$ gravity or chameleon theories have previously been performed by Oyaizu (2008); Li & Zhao (2009); Zhao et al. (2011). Because the highly nonlinear nature of Eq. (5) means that the code spends a substantial fraction of the computation time solving f_R , early simulations were largely limited by the box size or force resolution, or both. This work makes use of large-box $f(R)$ simulations performed by the ECOSMOG code (Li et al. 2012). ECOSMOG is an extension to the mesh-based N -body code RAMSES (Teyssier 2002), which is parallelised with MPI and can therefore have improved efficiency and performance than early serial simulation codes for $f(R)$ gravity. The technical details of the code are described in detail elsewhere, e.g., Li et al. (2012) and interested readers are referred to those references. We note that parallelised $f(R)$ simulation codes have recently been developed by other groups, e.g., Puchwein et al. (2013); Llinares et al. (2013). The simulations used for the void analyses in this work are

listed in Table 1. They all have the same values of cosmological parameters, summarised here as $\Omega_m = 0.24$, $\Omega_\Lambda = 0.76$, $h = 0.73$, $n_s = 0.958$ and $\sigma_8 = 0.80$, where $h \equiv H_0/(100 \text{ km/s/Mpc})$ is the dimensionless Hubble parameter at present, n_s is the spectral index of the scalar primordial power spectrum and σ_8 is the linear root-mean-squared density fluctuation measured in spheres of radius $8\text{Mpc}/h$ at $z = 0$. The background cosmology for all these models is the same as in the Λ CDM variant in practice (the difference caused by the different $f(R)$ model parameters is negligible). Therefore, the differences in these simulations only come from the modified gravitational law.

We call a group of Λ CDM, F6, F5 and F4 simulations with the same technical settings (e.g., box size and resolution) a simulation suite. All models in each simulation suite share the same initial condition generated using the Zel'dovich approximation at an initial redshift, $z_i = 49$. Although generally speaking the modified gravitational law also affects the generation of the initial condition (Li & Barrow 2011), in the $f(R)$ models studied here the fifth force is strongly suppressed at $z_i \geq 49$, and so its effects are negligible at the initial times. The use of the same initial conditions for all simulations in a suite means that the initial density fields for the Λ CDM and the $f(R)$ simulations share the same phases, and any difference in the void properties that we find at late times is a direct consequence of the different dynamics and clustering properties of $f(R)$ gravity.

3 VOID FINDING ALGORITHM

We use a void finder based on the one presented by Padilla et al. (2005, P05) with improvements centred on optimising the method, on improving its convergence for different mass resolutions and box sizes, and adapted to run on parallel computers. Our finder can be run either on the dark matter field or using dark matter halo tracers.

In the case of searching for voids in the dark matter field, the improved finder (iP05 from now on) follows the following steps:

(i) It searches throughout the simulation volume for regions of low density, performing a top-hat smoothing of the density field on a grid. We take all the grid cells with a density below a set threshold δ_{cell} as prospective void centres. We define a grid such that each cell contains on average 10 dark-matter particles so as to avoid being affected by shot noise that unnecessarily increase the number of prospective centres when this minimum number is lower. In the case when the detection of voids is done using haloes we adopt the same average number of objects in a cell (notice that since haloes trace peaks of the dark matter field, this is probably a conservative choice). We adopt a grid threshold $\delta_{\text{cell}} = -0.9$, i.e., only empty cells are prospective void centres.

(ii) We start measuring the underdensity in spheres of increasing radius about these centres until some void threshold, Δ_{void} , is reached. If the largest sphere about any one centre contains at least 20 particles, it is kept as a void candidate. This number provides the best stability of the method against resolution and boxsize changes. In almost all cases we adopt a value of $\Delta_{\text{void}} = -0.8$. However, for $z > 0$ we also adopt different thresholds that take into account the linear growth of perturbations until $z = 0$ (this will be indicated for each particular case). The void radius is defined as the radius of the under-dense sphere. As a result, the void density profiles typically reach the cosmic mean density quite far from the void radii.

(iii) The candidates are ranked in decreasing order of size, and we reject all spheres which overlap with a neighbouring sphere with

Table 1. Some technical details of the simulations performed for this work. F6, F5 and F4 are the labels of the Hu-Sawicki $f(R)$ models with $n = 1$ and $|f_{R0}| = 10^{-6}, 10^{-5}, 10^{-4}$ respectively. Here k_{Nyq} denotes the Nyquist frequency. The last column lists the number of realisations for each simulation.

models	L_{box}	number of particles	k_{Nyq} [$h \text{ Mpc}^{-1}$]	force resolution [$h^{-1} \text{ kpc}$]	number of realisations
ΛCDM , F6, F5, F4	$1.5h^{-1}\text{Gpc}$	1024^3	2.14	22.9	6
ΛCDM , F6, F5, F4	$1.0h^{-1}\text{Gpc}$	1024^3	3.21	15.26	1
ΛCDM	$250\text{Mpc}/h$	1024^3	12.82	3.8	1

a larger radius by more than a given percentage of the sum of their radii. This percentage will be treated as a free parameter: increasing the overlap percentage increases the size of the sample, which helps to obtain better statistics, but it also introduces larger covariances in the results, which could in the end lower the significance of a comparison between models. In the case of voids in the distribution of the dark matter field, we choose to use 10 percent overlap.

Following Ceccarelli et al. (2012), voids are classified into void-in-void and void-in-cloud objects depending on whether the accumulated overdensity at 3 void radii from the void centre is below or above zero, respectively, or simply by dividing our sample in different void sizes, since smaller voids contain larger fractions of void-in-cloud objects (see Ceccarelli et al. 2013; Cai et al. 2013; Hamaus et al. 2014, for examples).

When searching for voids in the distribution of dark matter haloes, the step (ii) above is slightly modified, where we now do not demand a minimum number of haloes within a void. This is due to the high significance of the peaks marked by haloes, which implies that a volume empty of haloes is the one with no peaks, and as such it is of interest to us. Furthermore, if for the same initial conditions the resolution of the simulation were improved, the haloes of the lower resolution simulation would again be found, though the dark matter particle positions would indeed change due to the change in the sampling of the smooth density field. Additionally, we will allow the percentage of void overlapping to vary from 50 to 0, in order to search for the optimal sample to distinguish between GR and $f(R)$ models.

Using haloes to identify voids is more practical observationally than using dark matter, but one has to face the challenge of sparse sampling. Especially, the centering of the spherical voids needs to be done more carefully since haloes only sparsely sample the density field. In particular, since a sphere can be defined by four points on its surface, a well-centred spherical void should contain four haloes, all living at a distance of exactly one void radius from the void centre. However, the precision of centering of our voids is of $0.3\text{Mpc}/h$, so we do expect some dispersion in the distance to the first four closest haloes. We assess the quality of our voids using this dispersion defined as

$$\sigma_4 \equiv \sqrt{\left\langle \left(\frac{d_i - \langle d_i \rangle_4}{\langle d_i \rangle_4} \right)^2 \right\rangle_4},$$

in which d_i is the distance from the void centre to the i -th halo, and $\langle \rangle_4$ denotes the average over the 4 closest haloes. The typical value for this parameter in our void samples is $\sigma_4 \simeq 0.05$, as shown in the inset of Fig. 5.

When using haloes as tracers, our void finder identifies voids with no haloes, but also allows voids to contain one or more haloes within its volume, as long as the threshold criterion, $\Delta_{\text{void}} = -0.8$, is met. Note that we have $\Delta_{\text{void}} = \delta n / \bar{n}$ when referring to threshold criterion for halo-identified voids, where n is the halo number

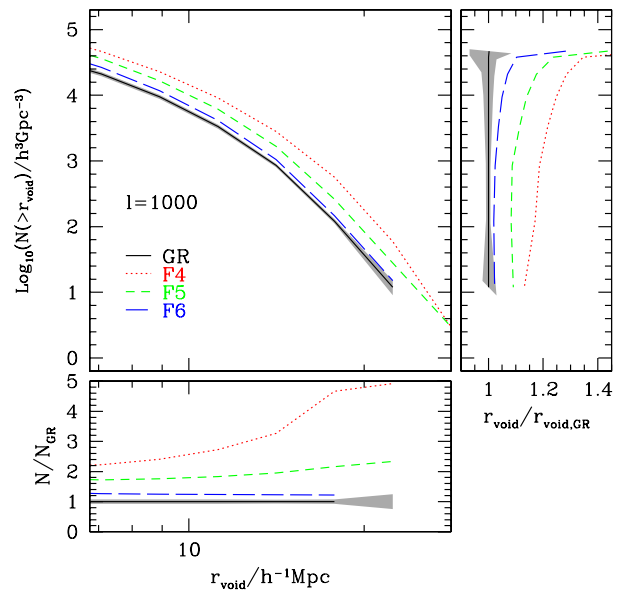


Figure 1. Void abundance as a function of void radius in real space, for the GR, F6, F5, and F4 simulations of $1000\text{Mpc}/h$ a side boxes (different line types indicated in the key). The shaded region shows the errors obtained from multiple realisations of a larger simulation. The lower subpanel shows the abundance ratio between the different models and GR, while the right subpanel shows the ratios between void radii at fixed abundances with respect to GR.

density; in contrast, for voids identified using the dark matter field, the threshold is defined as $\Delta_{\text{void}} = \delta\rho_m / \bar{\rho}_m$.

There are several routes to come closer to voids as would be identified with real galaxy catalogues. For example, one could simply weight each dark matter halo by the halo occupation number that corresponds to its mass. To do this, though, one needs the halo occupation distribution (HOD) parameters fit to observational data, and this is currently only available for ΛCDM (e.g. Zehavi et al. 2011). In order to make a consistent comparison between GR and $f(R)$ it would be necessary to first find the HOD parameters for the $f(R)$ cosmologies. Another possible avenue is to use semi-analytic galaxies, obtained by coupling a semi-analytic galaxy formation model to the merger trees extracted from the GR and $f(R)$ simulations. This approach is again not ideal because it assumes that the physics of galaxy formation is the same in both models, which may not be the case. Our present approach of using haloes as tracers is comparable to identifying voids in galaxy group catalogues, and as such is already applicable to current surveys.

4 VOID ABUNDANCE

We have discussed that voids can be identified using either the dark

matter field or biased tracers such as dark matter haloes or galaxies. Although the latter are more directly related to real observational data, the former is of more theoretical interest, as it directly reflects how dark matter clusters under the action of modified gravitational laws. In this section, we show void abundances found in both ways.

4.1 Voids identified using the dark matter field

We use the iP05 finder on the dark matter field of the 1000 Mpc/h-a-side boxes for the GR, F6, F5 and F4 simulations. The resulting abundances as functions of void radius are shown in Figure 1. We show the results for the voids identified using positions in real space for the dark-matter particles. In order to determine the minimum void radius above which our void sample is complete in these simulations, we run the void finder in smaller 250 Mpc/h simulations with the same number of particles, i.e. with 64 times the mass resolution, and find that the abundances of the small and large simulations are consistent down to a void radius of 7 Mpc/h. Therefore, from this point on, we will concentrate on voids of at least this size unless otherwise stated.

As can be seen in the main panel of Figure 1, the abundance of voids at a fixed radius increases from GR to $f(R)$ gravity, as expected due to the action of the fifth force that tends to point towards the void walls (Clampitt et al. 2013), which is stronger progressing from F6 through F5 to F4. Dark matter voids in $f(R)$ models therefore grow larger and their void abundances greater.

The lower subpanel shows the ratios of the abundances of the modified gravity models with respect to GR. The F4 model shows the strongest differences from GR, with abundances higher by factors of $\sim 1 - 4$, and larger for larger void radii. The right subpanel shows the ratio of void sizes at fixed void number densities, where the roughly constant ratios indicate that the differences between the models are almost due to larger void sizes for the modified gravity models compared with GR, except at high number densities where the ratios start to increase steadily. We checked the results in red-shift space and found very small difference from what is shown in Fig. 1.

The shaded region in Fig. 1 shows the error in the GR abundances, and the lower panel shows that the GR and F6 abundances are significantly different, by at least 3 standard deviations (3σ) up to void radii $\simeq 20$ Mpc/h. To estimate these, we have used larger simulations of 1500 Mpc/h aside, for which there are a total of 6 realisations for each model. In order to estimate errors for the cubic Giga-parsec simulations, we simply compute the dispersion of abundances measured in 1000 Mpc/h-aside subboxes of the large simulations. We use these errors instead of Poisson estimates since the dispersion from multiple realisations is more representative of the cosmic variance. Fig. 2 shows different estimates of cumulative abundance errors for the GR (solid) and F4 (dotted lines) models for the large simulations. The black lines correspond to the Poisson estimates of the errors and the red lines to the dispersion of the different realisations using the full simulation volume. These two estimates of error are very different for void radii < 20 Mpc/h; this is the reason why we adopt the realisation dispersion. The other lines show the dispersion of 1000 (blue) and 250 Mpc/h (green) aside subboxes. As can be seen, decreasing the volume to 1 (Gpc/h)³ does not increase the errors as it would be expected from Poisson fluctuations. The errors for the smaller volume of 250 Mpc/h are much larger, on the other hand.

As mentioned in the introduction, the main motivation to study voids in modified gravity models is that the abundances of voids are more sensitive to the fifth force than the halo mass functions. The

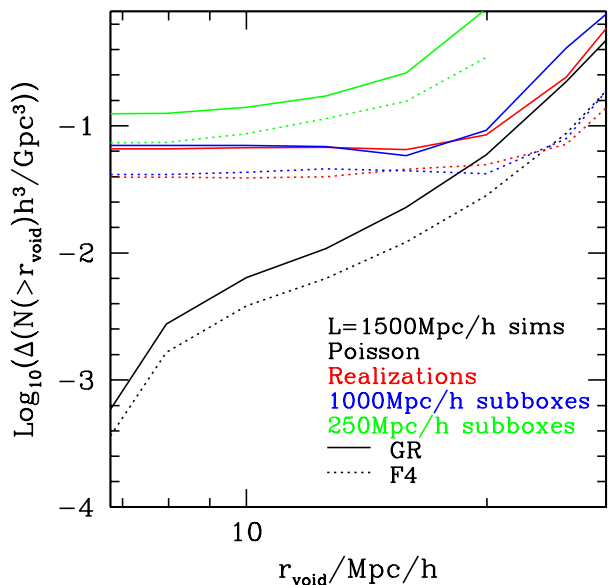


Figure 2. Void abundance errors obtained from 6 realisations of our 1500 Mpc/h a side simulations. We show errors arising from assuming Poisson fluctuations (black), the dispersion from the realisations for the full simulation volumes (red), and for two smaller sub-volumes (blue and green), for the GR and F4 models (solid and dotted, respectively).

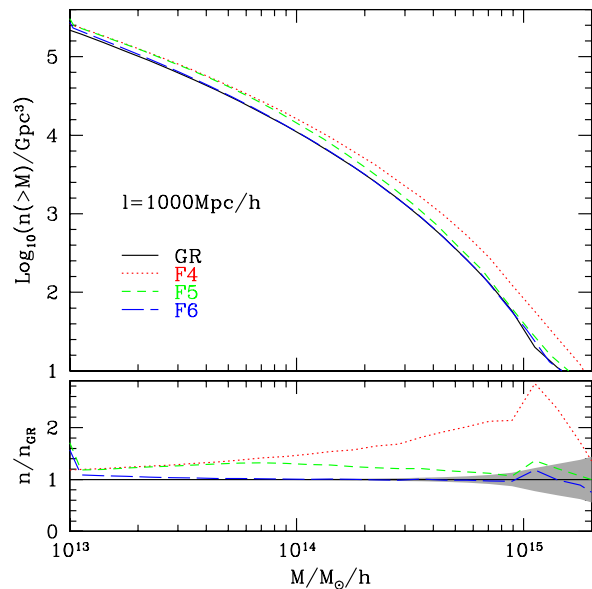


Figure 3. Cummulative halo mass functions for the GR, F6, F5, and F4 models (different line types and colours as indicated in the key). The shaded area shows the Poisson error in the GR model. The lower panel shows the ratio between the different $f(R)$ models and GR, using the same colours as in the top panel.

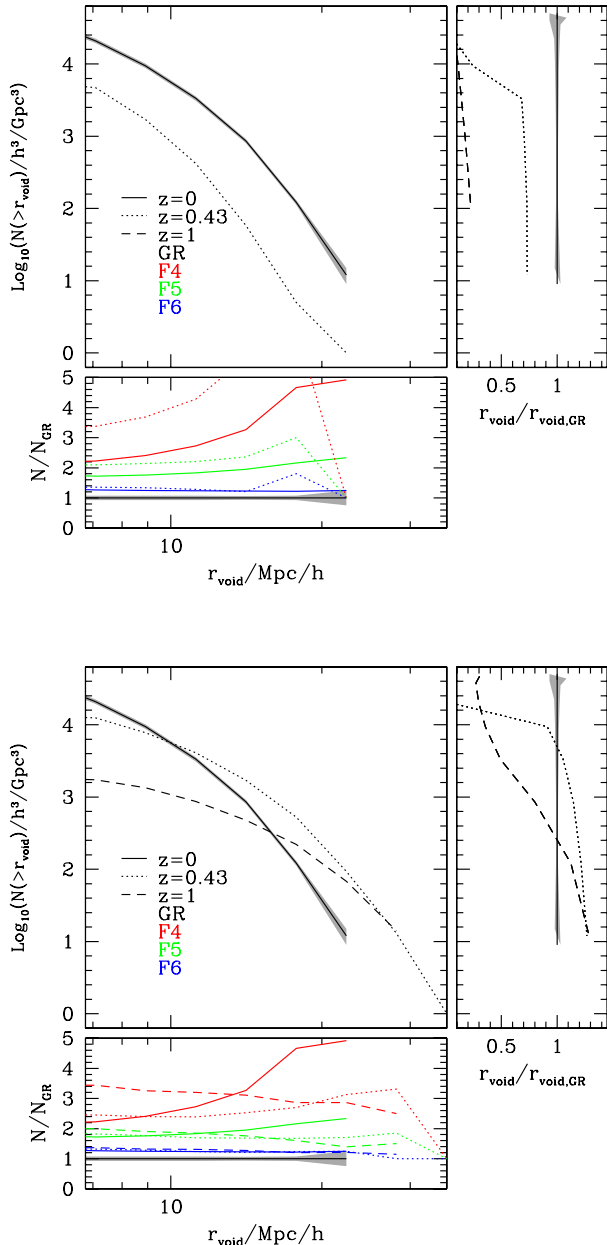


Figure 4. Void abundances at different redshifts (solid, dotted and dashed as the redshift increases), adopting the same over-density threshold of $\Delta_{\text{void}} = -0.8$ (top panels), and a threshold which evolves according to the linear perturbation growth, $\Delta_{\text{void}} = -0.8, -0.65$ and -0.51 for $z = 0, 0.43$ and 1.0 , respectively (bottom panels). For clarity, the main panels only show the results for the GR simulation. The lower subpanels are as in Figure 1. The right subpanels show the ratio between GR void radii at fixed abundance and redshift, with respect to GR voids at $z = 0$.

latter is shown in Fig. 3, where it can be seen that the change of the halo abundance as we move from GR through F6 and F5 to F4 is complicated. Furthermore, the F6 model shows virtually no differences from the GR abundances down to masses $\simeq 10^{14} h^{-1} M_{\odot}$, whereas the void abundance is significantly different between these two models across the range of void sizes reliably accessible in our simulations.

Given that large surveys are shifting toward higher redshifts, we also measure the abundance of voids at two higher redshifts,

$z = 0.43$ and 1 . Since fluctuations grow with time one can either use a fixed density threshold to identify voids at different redshifts, or make it evolve with the growth of fluctuations. We adopt both approaches and show the results in Fig. 4, where the top panels show the results for a fixed threshold of $\Delta_{\text{void}} = -0.8$, and the bottom panel for an evolving threshold following the linear growth of fluctuations for the cosmology of the GR simulation (differences are almost indistinguishable for the modified gravity models adopted here), with $\Delta_{\text{void}} = -0.8, -0.65$ and -0.51 for $z = 0, 0.43$ and 1.0 , respectively. To improve clarity the main panels only show the results for the GR simulations, but the lower subpanels show the ratio of abundances with respect to GR (colours for different models, solid, dotted and dashed line types as the redshift increases). The right subpanels show the ratio between void sizes at fixed abundance for GR alone, with respect to $z = 0$.

The main panels of Figure 4 show that a fixed threshold effectively produces much smaller samples at $z = 0.43$ and 1 , to the point that for the latter the number of voids is too small to appear in the figure. This is because very empty regions, e.g., $\Delta_{\text{void}} \leq -0.8$, only form at late times. An evolving threshold, on the other hand, produces higher abundances of large (comoving size) voids, but a smaller total number of voids (the intersection of the lines with the y -axes). This may be due to the use of linear theory to rescale the threshold, which is likely to be over-evolving the actual growth of fluctuations because the evolution of under-densities tends to be slower than the linear theory result. The right subpanels show that the main difference in the abundance of voids for a fixed threshold can be absorbed by a constant factor in the void radius: $z = 0.43$ voids are $\simeq 0.7$ times smaller than those at $z = 0$, whereas $z = 1$ voids are ~ 5 times smaller than at $z = 0$. The constant shifts of the void abundance functions among different epochs reflect a simple picture for the evolution of voids, which is captured by our void algorithm. More in-depth study of the evolution of void abundance is needed to shed light on the physics behind.

Regarding the differences between $f(R)$ gravity and GR, at higher redshifts the abundances are higher in the F6 to F4 models with respect to GR, by factors similar to those at $z = 0$ (see the lower subpanels). However, if a fixed density threshold is adopted, the number of voids will be smaller and the errors larger, making the difference between F6 and GR less significant. This should not be a problem if the evolving threshold is adopted.

4.2 Voids identified using dark matter haloes

In real observations, voids are usually identified by using tracers of large-scale structure, such as galaxies. In general, to compare simulations with observational data, one has to generate galaxy mocks. However, Padilla et al. (2005) has shown that the properties of voids found from mock galaxies are compatible with those of voids identified from dark matter haloes. Also, as mentioned above, the use of HOD or semi-analytic galaxy mocks incur further complications in the framework of $f(R)$ gravity, the remedy of which is beyond the scope of the present work. Therefore, as an initial step, we only use voids found using dark matter haloes.

We apply our void-finding algorithm to the halo field in our simulations of GR and $f(R)$ gravity. The dark matter haloes are identified using the spherical overdensity code AHF (Knollmann & Knebe 2009). We use haloes with the mass cut-offs $M_{\text{min}} = 10^{12.8} M_{\odot}/h, 10^{12.868} M_{\odot}/h, 10^{12.865} M_{\odot}/h$ and $10^{12.842} M_{\odot}/h$ for GR, F4, F5 and F6 simulations respectively, where M_{min} is the minimal halo mass of the catalogue. M_{min} is chosen to ensure that the haloes contain at least 100 particles each,

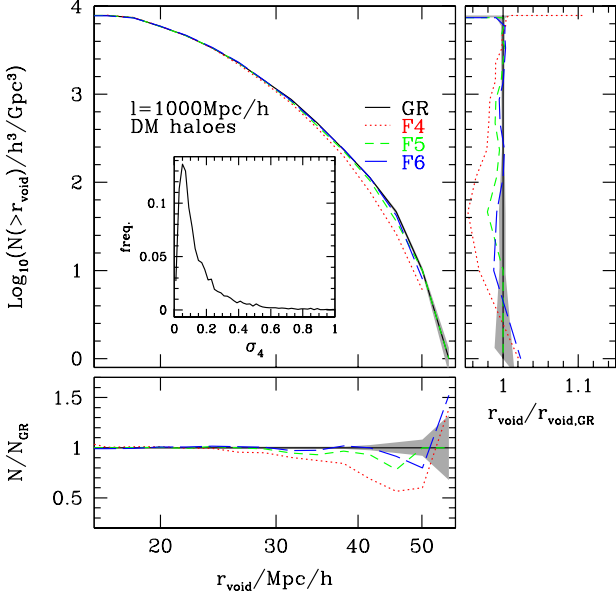


Figure 5. Void abundances resulting from using dark matter haloes as tracers of the density field. Panels and lines are as in Figure 1. The inset in the main panel shows the distribution function of σ_4 , the relative dispersion in the distance to the first four haloes above the void density threshold, for GR; a small value of σ_4 indicates a well centred void.

and the slight differences in the M_{\min} values for different models is to make sure that the halo number densities among different models are the same. This is necessary because it is likely to find different population of voids if the tracer densities are different, even for the same simulations. By using the same number densities of tracers for different models, we make sure that the differences among void populations are purely due to structure formation of different models. As mentioned in the previous section, we explore the results in the halo defined void statistics using different overlap percentages of 50 to 0, and study the effects this choice has on the significance of the comparison between GR and $f(R)$ statistics.

The resulting void abundances for halo voids with 20 percent overlap are shown in Fig. 5. The results have several important features. First, since haloes are highly biased tracers of dark matter, and are mainly distributed along walls and filaments, voids found in this way are more abundant and larger than those identified from the dark matter field. Second, the difference of the void abundances amongst different models is much smaller than in the case of dark matter voids, and this suggests that it is much more difficult to use the observed void abundance alone to constrain $f(R)$ gravity. This is possibly a consequence of the fact that haloes are highly biased tracers of the underlying dark matter field and have formed from the high peaks of the initial density field: while the fifth force can drastically change the clustering of dark matter, its effects on haloes are weaker and a density peak which corresponds to a halo in $f(R)$ simulations is also likely to have formed a halo in the GR simulation. Third, and most interestingly, we notice that voids larger than $r_{\text{void}} \simeq 25 \text{ Mpc}/h$ are less abundant in $f(R)$ models than in GR.

This last observation is counter intuitive and seems to be inconsistent with the physical picture that voids grow larger and emptier in $f(R)$ gravity because the fifth force points towards the edges of voids (Clampitt et al. 2013). To check this, we use the void centres found in the GR simulation and count all the haloes residing within the GR void radius, for the different models. Two examples

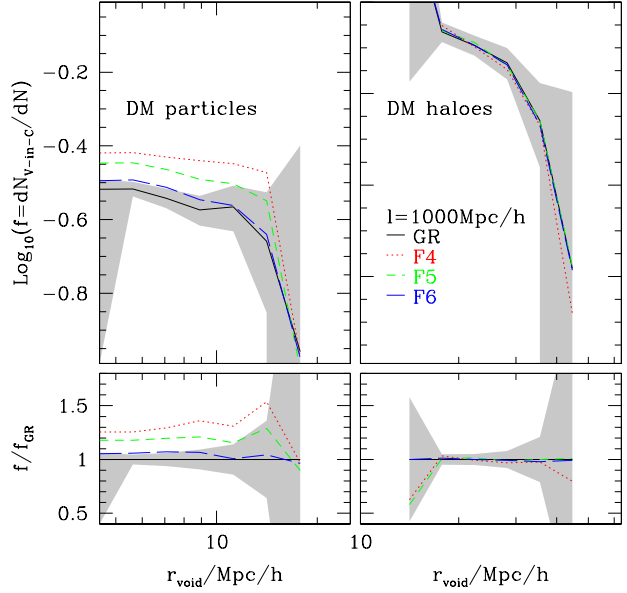


Figure 7. Fraction of void-in-cloud voids as a function of void radius, for the GR, F6, F5 and F4 models (different line types as shown in the key). The bottom panel shows the ratio of the fractions with respect to GR.

comparing F4 and GR halo number counts in this way are presented in Fig. 6. It is interesting to note that there are more haloes found in the $f(R)$ simulation within the same void radii, even when the minimal halo mass cut is lower for GR (as indicated by the dotted lines). This is likely due to the stronger environmental dependence of halo formation in $f(R)$ models (Li & Efstathiou 2012). The fifth force in $f(R)$ gravity in these large under-dense environments is stronger, which makes it more likely for haloes of the same mass to form in $f(R)$ than in GR. The halo number density within the same sphere is therefore smaller in GR than in $f(R)$, making it easier to pass our void selection criteria in the former case. We can also see that the masses of haloes in F4 are larger. Thus even if we make the same M_{\min} cuts for both simulations, the same phenomenon that the largest voids in GR are bigger than in $f(R)$ gravity would still be present, as we have checked explicitly.

In all cases the samples of voids are well centered as evidenced by the σ_4 values obtained for the voids. The inset in Fig. 5 shows the distribution of σ_4 for GR; as can be seen it peaks at $\sigma_4 \simeq 0.05$, indicating an accuracy of better than 5% the void radius in its centre. The histogram of σ_4 has a long but very low tail extended to larger values. This suggests that the majority of voids identified are perhaps close to spherical. Only a small subset of voids has large value of σ_4 , which are perhaps very different from spherical or are fake voids. With the σ_4 value for each void, we can control the quality of our void sample. We will later use cuts in this parameter to select subsamples of improved statistical value.

In summary, dark matter void abundances are greater in $f(R)$ than that in GR. In contrast, halo voids show the opposite trend, that relatively large voids are less abundant in $f(R)$ gravity than in GR, and their differences are much smaller than in the case of dark matter voids. This rings an alarm that voids identified from tracers are very different from those from dark matters. We will see this further in our paper in terms of void profiles.

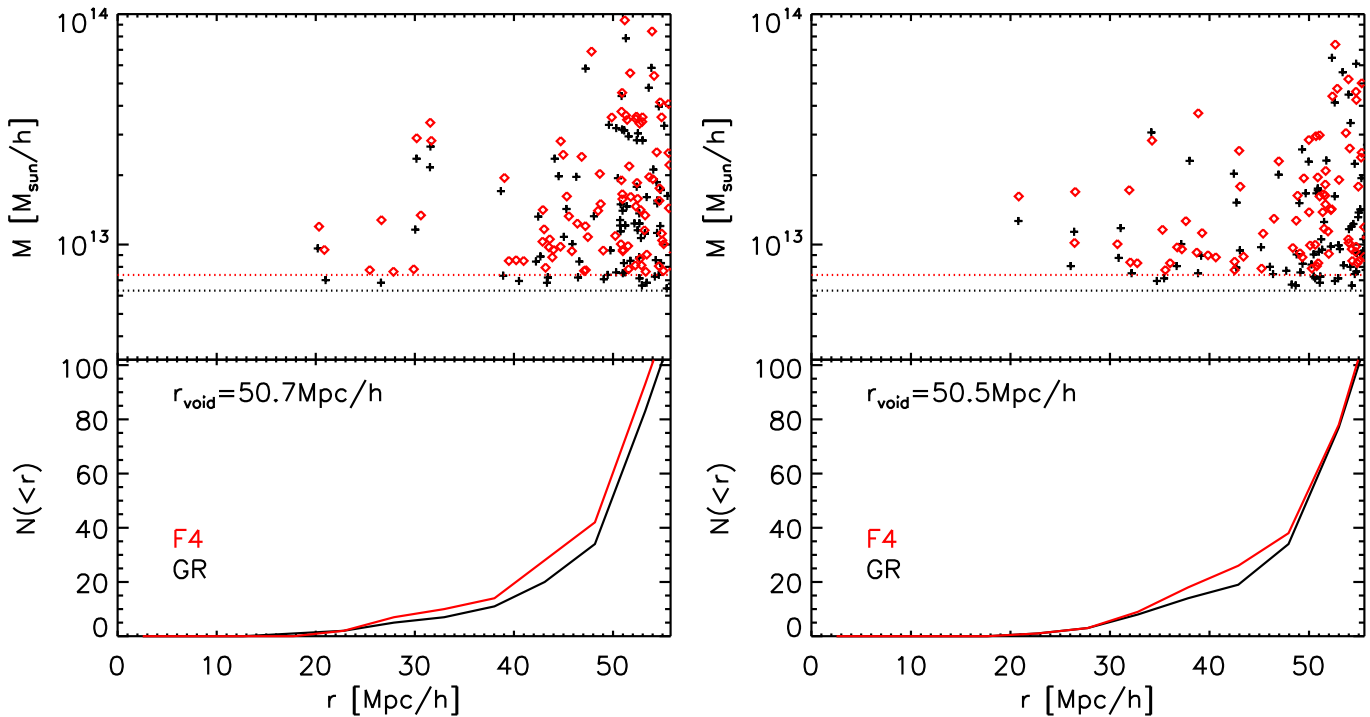


Figure 6. The two largest voids found in our GR simulations using haloes above $10^{12.8} M_{\odot}/h$, as indicated by the black-dotted lines. On the top panels, each black cross represents the radial distance of a halo from the void centres versus the halo mass. The red diamonds are the haloes found in the same comoving radius from the same GR void centres, but from the simulation for the F4 model; the halo mass cut for this model is indicated by the red dotted line. The slight differences between the black dotted and red dotted lines are to make sure that the number density of haloes between these two models are the same. Bottom panels show the cumulative number of haloes from the centre of the GR voids. The F4 curves being above the GR curve suggests that more haloes form within these void regions in F4 than in GR.

4.3 Void-in-cloud frequency

The effect of the fifth force in $f(R)$ gravity makes voids emptier, but this in turn could result in changes in the frequency of voids that form within over-densities, i.e. of void-in-cloud voids (Sheth & van de Weygaert 2004). With our adopted criterion to separate void-in-clouds we measure their fraction as a function of void radius, and show the result in Figure 7.

The left panel shows the results for voids identified using the dark matter particles, and the right panel corresponds to when using dark matter haloes as tracers of the density field. As can be seen, the fraction of void-in-clouds in the dark-matter density field increases from GR through F6 and F5 to F4. For the latter, this fraction is ~ 30 percent higher than for GR, almost constant with void radius. The differences are smaller, of only ~ 5 percent for F6, making this a difficult test on its own to separate $f(R)$ gravity from GR, but that can provide further constraining power when used in conjunction with abundances, and also with void profiles, a subject we will turn to in the next section.

When using dark-matter haloes to identify voids (right panel), the fraction of void-in-clouds is substantially higher than for voids identified using dark matter particles. However, the differences between the $f(R)$ models and GR all disappear as in the case of halo void abundances.

The fact that $f(R)$ gravity produces more voids-in-clouds reflects the fact that in $f(R)$ gravity, underdense fluctuations in the overdense environments are more likely to develop into voids that are selected by our algorithm, because the repulsive fifth force is the stronger for voids-in-cloud (Clampitt et al. 2013): the consequence of this is more voids are generated in overdense regions. Note that

the higher void-in-cloud frequency is mainly true for dark matter voids, but not obvious for halo voids: this is probably due to the sparse sampling of haloes.

5 VOID PROFILES

We have seen from the above section that void abundance is not a particularly powerful probe of $f(R)$ gravity in reality. In this section, we shall study the other basic property of voids, their profiles, and see whether stronger constraints can be obtained here. We will look at both the density and velocity profiles of voids.

From this point on we will only use voids identified in the halo fields for two reasons. The first is to mimic observational data that consists of galaxies. The second is related to the findings from the previous section: as results using haloes as tracers produce smaller differences between $f(R)$ gravity and GR, this choice will provide the minimum possible difference that would need to be detected to tell apart these different models.

We start from the halo void catalogue that allows 0-50% overlapping with neighbouring voids. The 50% is the ratio of the distance of two void centers versus the sum of their radii. For some extreme cases where one void is much smaller than the other, the small ones can still be a sub-void of the larger one, and they both pass our selection criteria. To avoid this, by default, we also exclude sub-voids that are 100% contained by a larger voids. We also exclude voids with shape parameter $\sigma_4 > 0.2$ to make sure that most of them are close to spherical. In general, changing these criteria does not affect most of our results qualitatively, but quantitatively, it may. We will address this in more detail in section 5.2

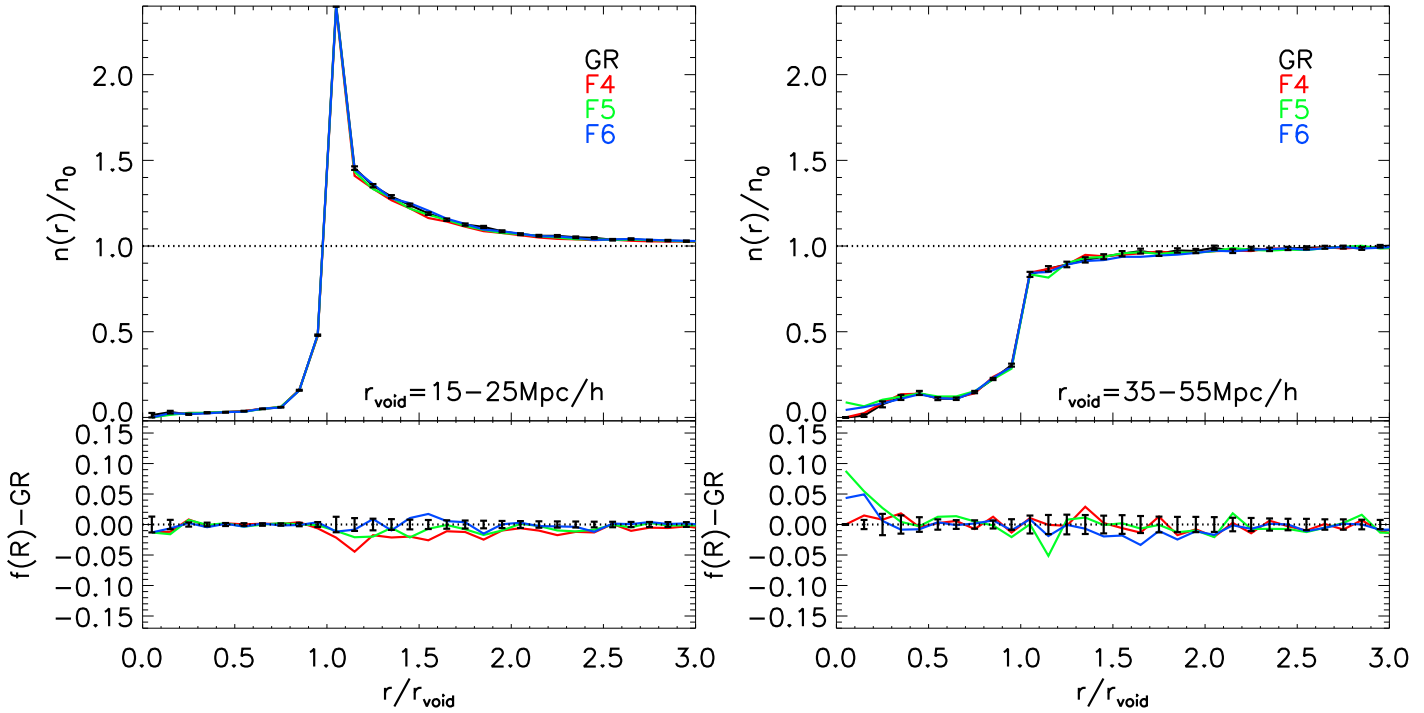


Figure 8. Top panels: void density profiles measured using haloes above the minimal halo mass of $M_{\min} \sim 10^{12.8} M_{\odot}/h$ from simulations of different models as labelled in the legends. M_{\min} is slightly different from $10^{12.8} M_{\odot}/h$ in the $f(R)$ models so that the number of haloes for different models are the same (see the text for more details). Error bars shown on the black line (GR) are the scatter about the mean for voids at $15 \text{ Mpc}/h < r_{\text{void}} < 25 \text{ Mpc}/h$ (left) and at $35 \text{ Mpc}/h < r_{\text{void}} < 55 \text{ Mpc}/h$ (right) found within the $1(\text{Gpc}/h)^3$ volume. There are [6038, 5946, 6096, 6307] (left) and [296, 323, 319, 261] (right) voids in GR, F6, F5 and F4 models passing the selection criteria. Bottom panels: differences of halo number density profiles of voids between $f(R)$ models and GR.

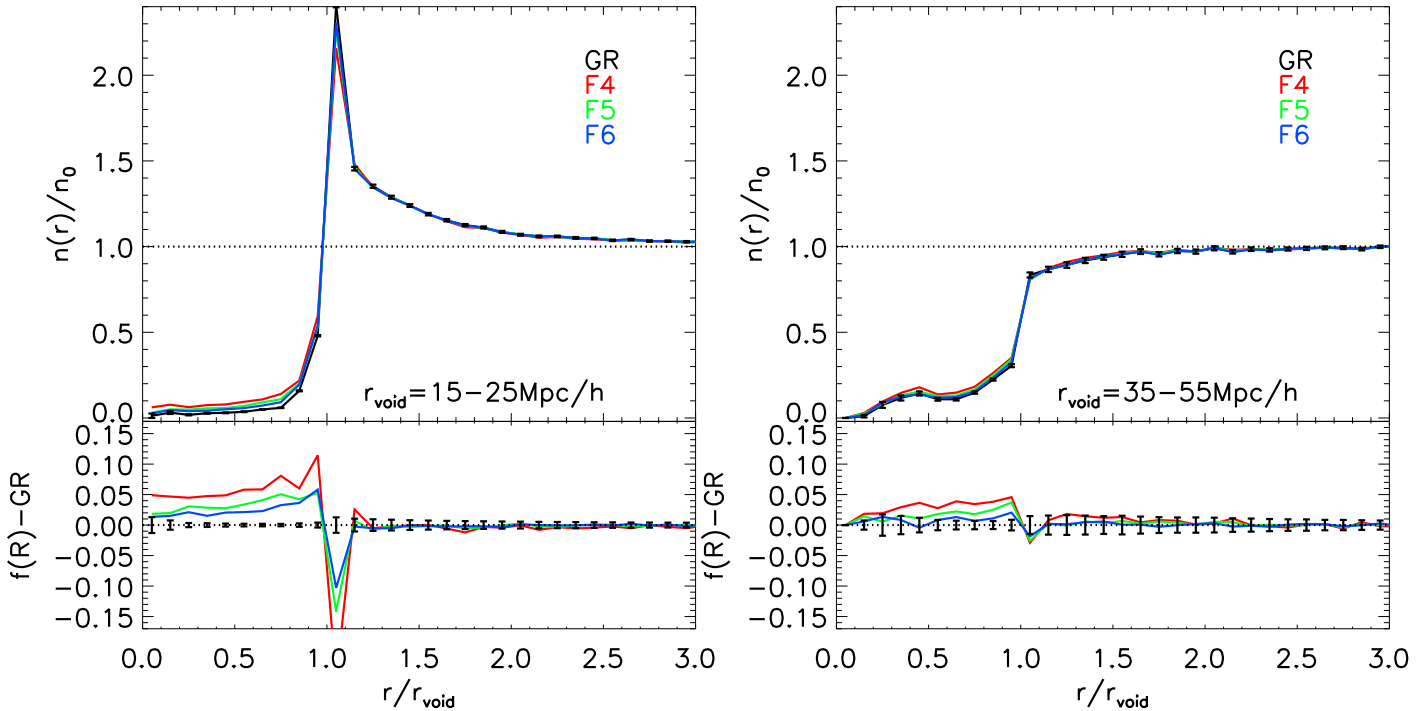


Figure 9. Similar to Fig. 8, but showing the halo number density profiles from using the void centers from the GR simulation and applying them to measure the profiles for halo catalogues of $f(R)$ models.

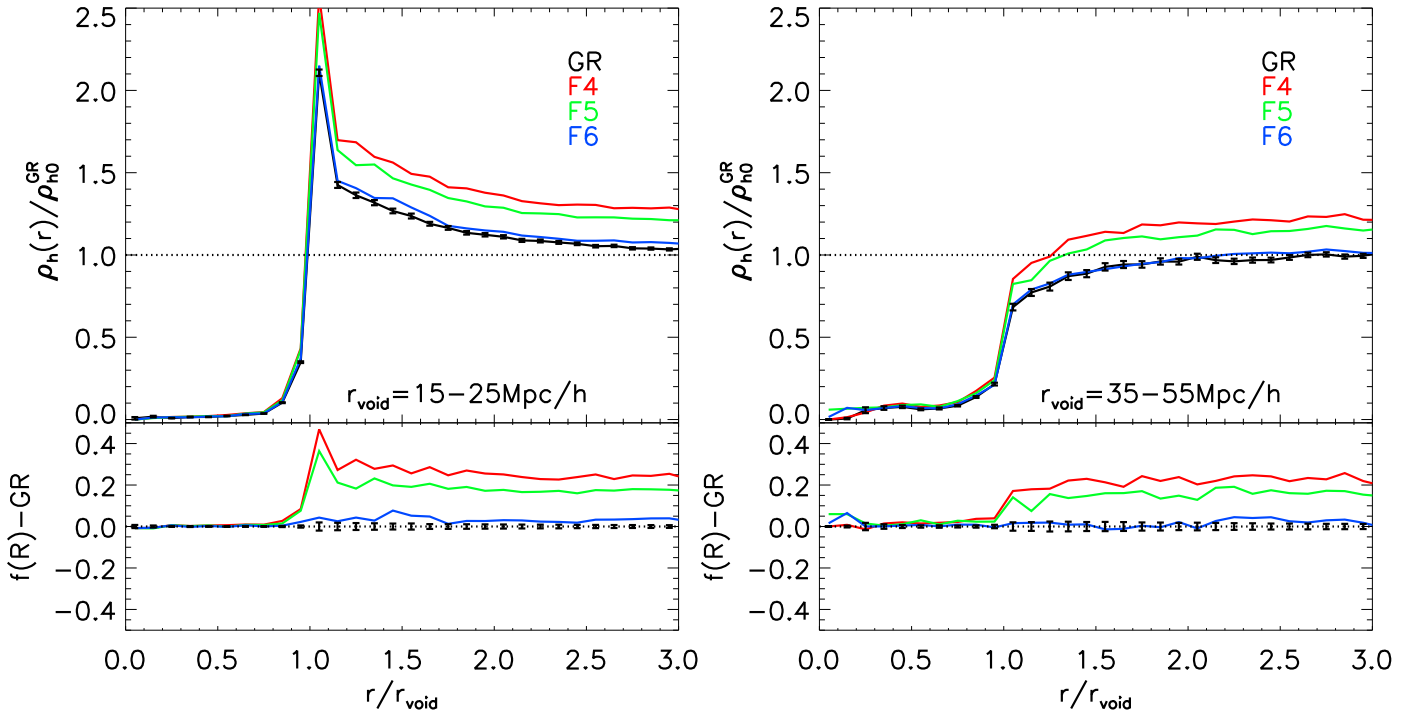


Figure 10. The void profiles for the mass contained in haloes. For better illustration, the profiles are normalized by a common denominator, the mass density of haloes above M_{\min} in the GR simulation.

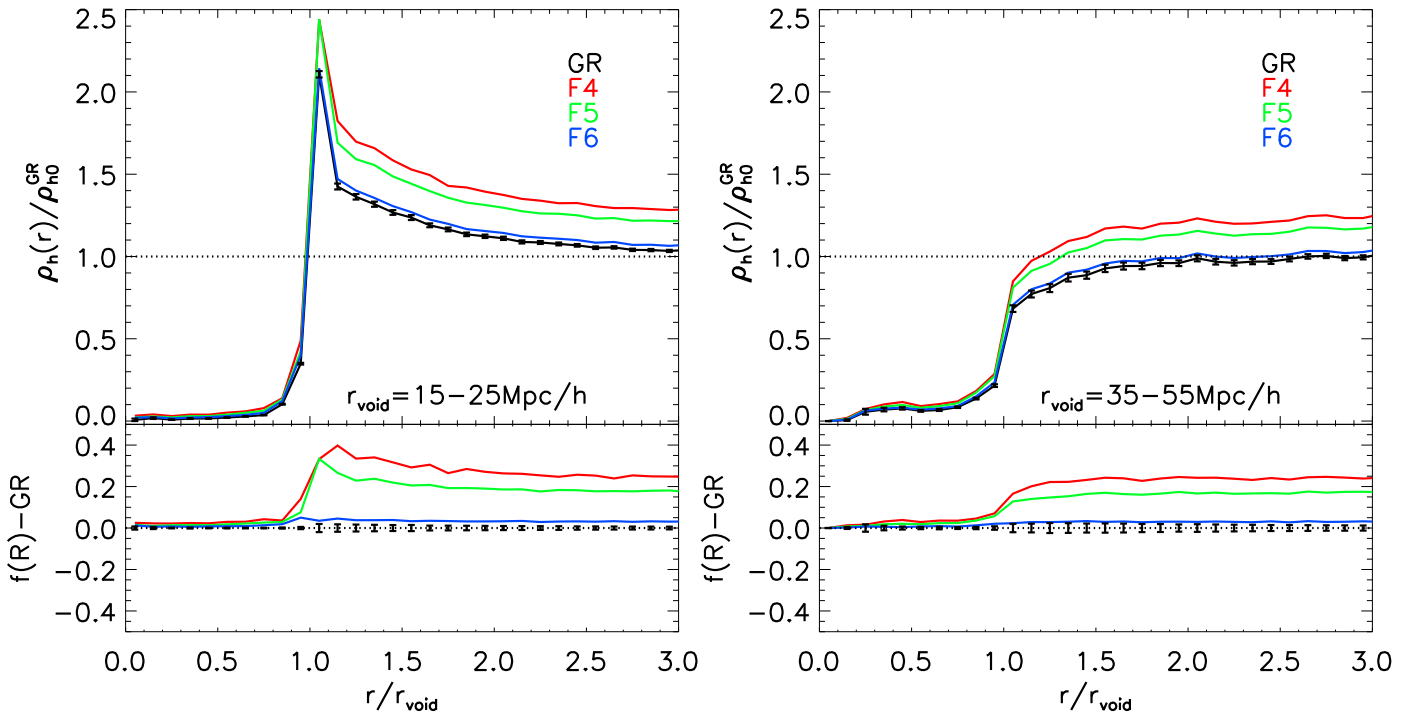


Figure 11. The same as in Fig. 10 but showing results from using void centers found in the GR simulation to measure the profiles in all models.

5.1 Void density profiles

5.1.1 Halo number density profiles of voids

We first investigate whether there is any difference for the dark matter halo distribution around voids. This has direct observational im-

plications as one can simply use the observed tracers (galaxies and galaxy clusters) for this measurement (Padilla et al. 2005).

With void centres and radii found from halo fields, we count the number of haloes in spherical shells of the thickness of $0.1r_{\text{void}}$ from a given void centre and divide them by the comoving volume of each shell to obtain the halo number density profiles of voids. We

rescale each halo-to-void-centre distance by the void radius before stacking them. Results are shown in Fig. 8, where error bars show the scatters about the means for the void samples obtained from our 1 (Gpc/h)^3 volume within the radius ranges shown in the legends. Error bars are plotted only for the GR lines for simplicity; the sizes of error bars are similar for the other models, as we have checked explicitly. The radius ranges of 15 to 25 Mpc/h and 35 to 55 Mpc/h are chosen to represent approximately the two different types of voids, void-in-cloud and void-in-void (see Ceccarelli et al. 2013; Cai et al. 2013; Hamaus et al. 2014).

We find that all profiles have very sharp rising feature at r_{void} . For small voids (the left panel), there are striking over-dense ridges at $\sim r_{\text{void}}$, and the profiles decrease gradually with r to reach the mean number density at $r \sim 2.5r_{\text{void}}$. For large voids (the right panel), there is no clear over-dense ridge, and the profiles increase asymptotically towards the mean, before reaching it at $r \sim 1.5r_{\text{void}}$. The profiles of the small and large voids are qualitatively as expected for voids-in-cloud and voids-in-void (Ceccarelli et al. 2013; Cai et al. 2013; Hamaus et al. 2014), though there is no clear division in void size for these two types, as we have checked explicitly. In general, smaller voids have steeper profiles than larger ones, with more prominent over-dense ridges. For the very small voids in our catalogues, their over-dense ridges are so prominent that they overcompensate the halo number (or mass) deficit within r_{void} . This reflects itself as the inflow of mass towards the void centre beyond a certain radius, as will be shown in Section 5.3.

It seems that the halo number density profiles of GR and $f(R)$ gravity are extremely close to each other. This is not surprising for the following two reasons. First, our void finding algorithm requires the number density of haloes to satisfy the same density criteria of 0.2 times the mean, and we do not expect to find strong differences of void profiles at least within r_{void} , as shown in the bottom panels of Fig. 8. Second, we are using very massive haloes, which are density peaks, to define voids. Due to the chameleon screening mechanism, the fifth force is likely to be suppressed in over-dense regions, and this minimises the difference of structure formation from GR in over-dense regions. The difference in the halo number density profile, if any, would reflect mainly the difference of environmental dependence for structure formation among different models.

In general, each dark matter halo does not necessarily correspond to one galaxy. If one uses galaxies as tracers to find voids and measures the resulted galaxy number density profiles of voids, the number of galaxies occupied in each halo will put different weights to haloes with different masses. This could make the void profiles look different from those presented in Fig. 8. However, as shown by Padilla et al. (2005), the use of galaxies instead of dark matter haloes have small impacts on the measured void properties. Moreover, assuming that the weights are similar for the different models, the differences between $f(R)$ gravity and GR, which are the main concern of our study, should remain similar. We therefore do not intend to explore beyond using haloes for the present study.

Model differences in void profiles might not be seen if void profiles are self-similar, i.e., if voids in $f(R)$ models grow larger than those in GR without changing their shapes, the rescaled void profiles will look the same. In other words, when looking at voids within the same radius range in different models, one may be comparing different void populations. To check if this happens for the results in Fig. 8, we test using void centres found in the GR simulation to measure the halo number density profiles for $f(R)$ simulations. This makes sure that we are comparing the same void regions of the same initial conditions. Any differences from GR should be purely due to the different structure formation process in $f(R)$. Re-

sults are shown in Fig. 9. Interestingly, we find that voids are less empty of haloes in $f(R)$ models than in GR within r_{void} . To check if the differences are due to the slight difference in the minimal halo masses among different models, we have also used halo catalogues of the same M_{min} to measure the profiles, and the results shown in Fig. 9 are confirmed.

Naively, the fact that voids in $f(R)$ models are not as empty of haloes as in GR may seem counter intuitive and contradict the conventional picture of voids in chameleon models. For example, the analytical study of Clampitt et al. (2013) suggests that voids should expand faster hence become emptier in these models. However, it is important to recall that voids defined using tracers (haloes) may be very different from the actual dark matter voids. When looking at haloes, as we do here, the above conclusion is understandable and consistent with what has been shown in Fig. 6, namely in $f(R)$ models, the fifth force is likely to be unscreened in void environments, which makes haloes form earlier and become more massive. Voids therefore becomes less empty than in GR if they are defined using dark matter haloes of a similar M_{min} .

It is also noticeable from Fig. 9 that the over-dense ridges at $r \sim r_{\text{void}}$ in $f(R)$ models are not as sharp as in the GR case. There are two possible reasons for this. Firstly, since some of these void regions in $f(R)$ models are not corresponding to voids in GR, or having slightly different radii from their GR counterparts, including them for the stacking smears the ridge slightly.

Secondly, for same over-dense regions, especially at the over-dense ridges, the merger rate of haloes may be higher in $f(R)$ models with the help of the fifth force. This makes the number of haloes decrease in those particular regions. If this is true, one may also expect that the mass contained in $f(R)$ haloes above our selection criteria should be no smaller, if not greater than that in GR. To test this, we weigh each halo with its mass to obtain the void profiles of the mass contained in haloes. Results are shown in Fig. 10 and Fig. 11. They are the mass-weighted versions of Fig. 8 and Fig. 9. For better illustration, we have normalised the mass density profiles by a common denominator, which is the density of mass contained in haloes in the GR simulation. Comparing Fig. 8 and Fig. 10, it is clear that although the number density of voids are very close to each other among different models, the masses contained in $f(R)$ models are greater than that in GR. The differences in the mass-weighted profiles are essentially the difference of halo mass functions in these models. Interestingly, even for the case of Fig. 9 where the number density of haloes in $f(R)$ models are slightly smaller at the over-dense ridge, the mass contained in the haloes are still greater than that in GR (Fig. 11). The difference of the mass-weighted profiles from GR is even greater at the over-dense ridge shown on the left-hand panels. This supports our argument that in over-dense regions, small haloes merge to make large haloes in a more efficient way in $f(R)$ models.

Note that the numerical experiments shown in Fig. 9 and Fig. 11 are purely for the understanding of physics. It is not possible to use voids found in one universe to measure the void profiles of another. What we can observe should be something similar to Fig. 8, i.e., using tracers of a universe to measure the void profiles in the same universe. In this sense, we conclude that in $f(R)$ models, void profiles seen in halo number density are not distinguishable from the GR results. The situation may be different for dark matter profiles of voids. With this in mind, it is important to understand the connection between void profiles of halo number density and those of dark matter, which is to be addressed in the following subsection.

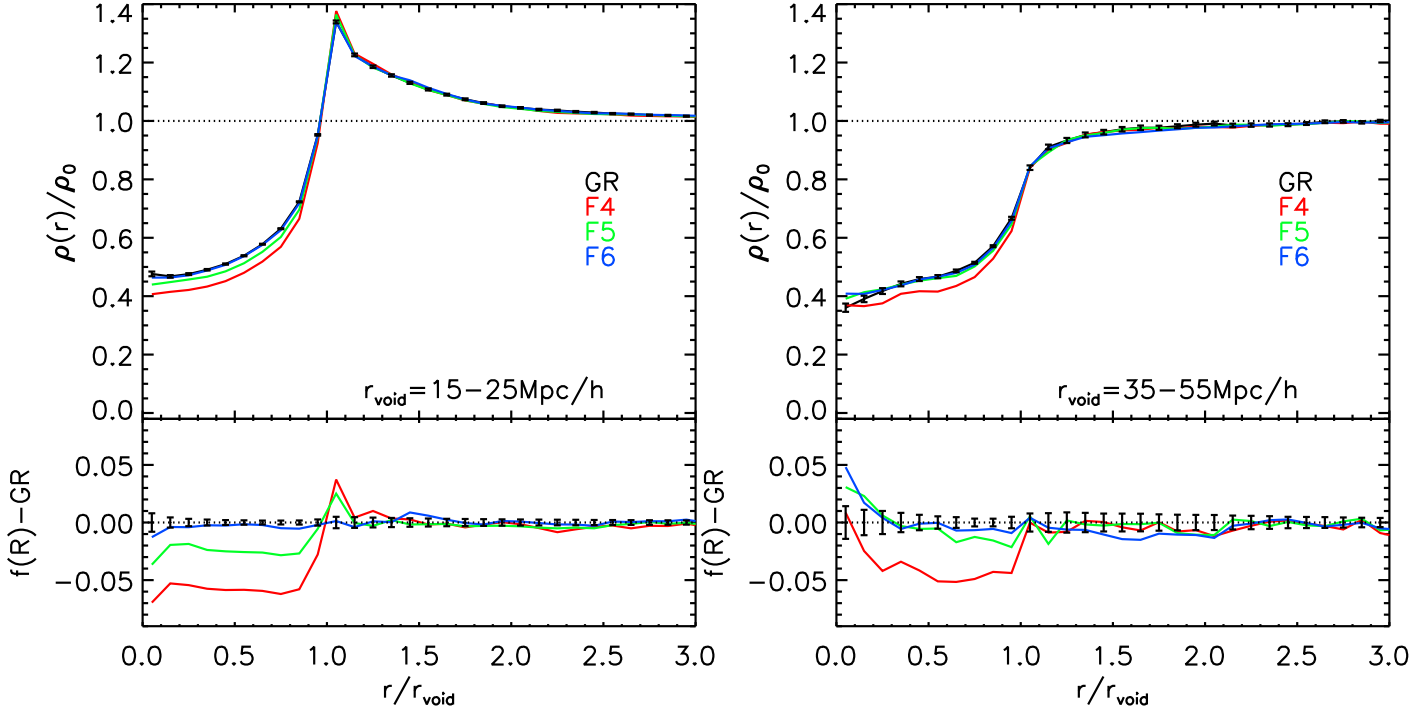


Figure 12. Similar to Fig. 8 but showing void density profiles measured using all dark matter particles from simulations of different models as labelled in the legends. Voids are defined using halo number density fields, which are the same as those being used to make Fig. 8.

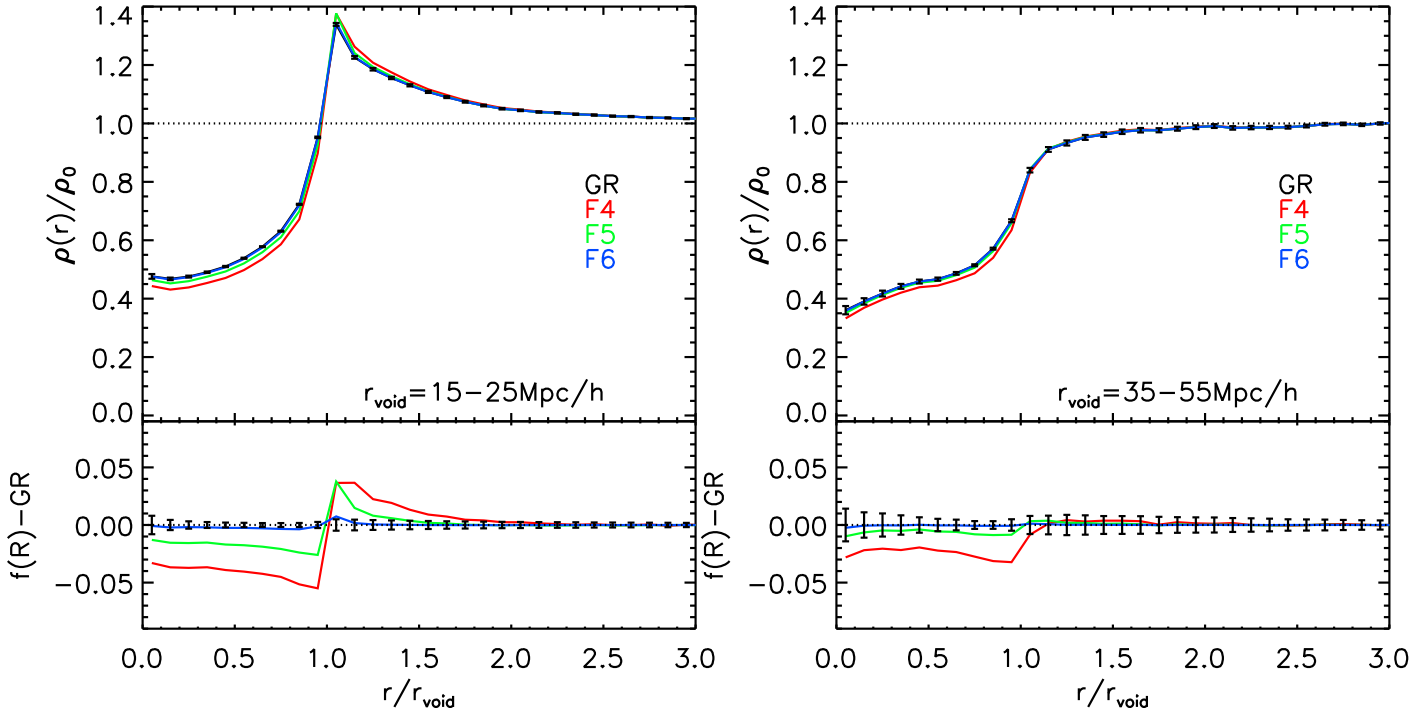


Figure 13. Similar to Fig. 12 but showing results using GR void centres to measure void profiles with simulations of different $f(R)$ models.

5.1.2 Dark matter density profiles of voids

With void centres and radii found from halo fields, we measure the dark matter density profile for voids using all dark matter particles, and rescale them in the same manner as for the halo number density profiles. Results are shown in Fig. 12, in which the error bars show

the scatter about the mean for the void sample selected from our 1 $(\text{Gpc}/h)^3$ volume within the radius ranges indicated in the legends. Again, we only show error bars for the GR lines for clarity.

As we have seen above, relatively small voids are much more likely to live in over-dense environments, while big ones are likely

to reside in under-dense environments. This can be clearly seen in Fig. 12 where small voids (left panel) have an over-dense ridge at $\sim r_{\text{void}}$, as expected for void-in-cloud, but not for large ones (right panel). These are qualitatively similar to the void halo number density profiles shown in Fig. 8. We have found very smooth density profiles with negligibly small error bars for all cases, which reflects the success of our void-finding algorithm in identifying voids using haloes that are associated with the underlying dark matter distribution.

For relatively small voids (left panel of Fig. 12), the dark matter density profiles have a very steep rising feature at approximately r_{void} , and cross the cosmic mean density at about the same place. This is somewhat surprising since the void radius is defined in halo field by looking for the maximal radius that has $n(< r)/\bar{n} \leq 0.2$. There is no *a priori* requirement in the definition of what the differential or cumulative density profile of dark matter should be like. It can be understood as that the halo field traces well the dark matter field in void regions.

More interestingly, it is noticeable that $f(R)$ voids are deeper than GR ones at $r < r_{\text{void}}$, and F4 is the deepest. At $r > r_{\text{void}}$, there is an indication that the over-density ridges are more prominent in $f(R)$ gravity than in GR. This can be more clearly seen in Fig. 13, where void profiles in different models are measured using void centres found in the GR simulation. Overall, we can conclude that voids in $f(R)$ gravity are emptier (in terms of dark matter) at $r < r_{\text{void}}$, even though the halo number densities of them are the same (cf. Fig. 8) or follow the opposite trend (cf. Fig. 9) in the same regime. Meanwhile, the over-density ridges may be slightly more prominent in $f(R)$ than in GR, even though it is just the opposite for the halo number density profiles (cf. Fig. 9, lower left panel).

The behaviour of dark matter density profiles are now in good agreement with our expectation for $f(R)$ model. Theoretical calculations have found that the fifth force in void regions is repulsive in these models, driving the expansion of walls of voids to go faster, and making voids emptier than in GR (Clampitt et al. 2013), which is what we see in Figs. 12 and 13.

The situations for relatively large voids (the right-hand panels of Fig. 12 and Fig. 13) are similar to that of the small ones except that there is no over-dense ridge for the void profiles. After rising sharply at $r \sim r_{\text{void}}$, the profiles gradually approach to the cosmic mean, before eventually reaching it at $\sim 1.5 r_{\text{void}}$. The differences among different models for large voids are also somewhat smaller, especially when the void profiles in all models are calculated using GR void centres (Fig. 13). This agrees with the analytical calculations of Clampitt et al. (2013) that the model differences in terms of void expansion is greater in voids-in-cloud than voids-in-void.

The good agreement between Figs. 12 and 13 suggests that the differences we find in Fig. 12 is physical. Nevertheless, the test of Fig. 13 is a thought experiment that does not happen in real observations. If we select voids with certain range of radius, their stacked profiles would encode the differences of void population as well as their evolution history. In this sense, results shown in Fig. 12 have more practical meaning.

In summary, the results of this subsection unveil the complexity of voids in $f(R)$ gravity. There are clear differences between the profiles of voids identified using tracers and those identified using dark matter. This makes it more challenging to place observational constraints. In the next subsection, we will explore the possibility of using weak gravitational lensing of galaxies by voids to constrain these models. Although observationally the direct identification of voids can only be done using tracers (haloes in our case), the lensing signal generated by voids are associated their underlying dark

matter distribution. Consequently, the combination of the two may provide perspectives of tighter constraints on $f(R)$ gravity.

5.2 Lensing tangential shear profiles

The dark matter profile shown in Fig. 12 can in principle be measured using weak gravitational lensing. Voids defined using tracers (haloes or galaxies) are closely associated with density decrements along the line of sight, as mentioned in Section 5.1. The deflection of light propagating through voids causes distortions to the shapes of background galaxies. The weak lensing shear signal of the background galaxies can be used to measure the matter distribution associated with the foreground voids (Amendola et al. 1999; Krause et al. 2013; Higuchi et al. 2013). This technique is similar to using galaxy-galaxy lensing to measure the density profile of dark matter haloes. The key quantity that connects observations and theoretical predictions is the tangential shear γ_t of the shape of the background galaxies. It is proportional to the excess of projected mass density along the line of sight,

$$\Delta\Sigma(R) = \gamma_t \Sigma_c = \Sigma(< R) - \Sigma(R), \quad (16)$$

where Σ_c is the geometric factor defined as

$$\Sigma_c \equiv \frac{c}{4\pi G} \frac{D_A(z_s)}{D_A(z_l)D_A(z_l, z_s)(1 + z_l)}. \quad (17)$$

Here $D_A(z_s)$ and $D_A(z_l)$ are the angular diameter distances from the observer to the source and the lens respectively, and $D_A(z_l, z_s)$ is the angular diameter distance between the lens and the source. $\Sigma(R)$ and $\Sigma(< R)$ are the projected surface densities around the centre of a void at the projected distance of R and within R . They are related to the cross-correlation function of void centres and dark matter via:

$$\Sigma(R) = \bar{\rho} \int [1 + \xi_{vm}(\sigma, \pi)] d\pi, \quad (18)$$

where $\xi_{vm}(\sigma, \pi)$ is the 2D cross-correlation function of void centres and dark matter. σ and π are the transverse line-of-sight separation and line-of-sight direction. For simplicity, we drop the $\bar{\rho}$ factor and work on dimensionless quantities. $1 + \xi_{vm}(\sigma, \pi)$ is essentially the 2D density profile of voids. To increase the signal-to-noise, we do a similar stacking as for the 1D profiles. Each void is rescaled by its radius before stacking. We have bins along the σ and π directions of width of $0.1 r_{\text{void}}$, and use Eq. (18) to integrate along the line of sight up to $2 r_{\text{void}}$, where the density comes back very closely to the background (see Fig. 12). Results are shown in Fig. 14. For simplicity, we show the profiles from stacking all voids in our 1 (Gpc/h)³ simulation box. The tangential shear signal peaks at $r \sim r_{\text{void}}$ where the 1D matter density profiles are the steepest. This is expected as $\Sigma(< R) - \Sigma(R)$, and is sensitive to the slope of the density profile. Close to the centre of void, or further away from the void, the density profiles are relatively flat, hence the tangential shear signal is small. But the signal can still be significant at a few times the void radius, as shown in the left-hand panel of Fig. 14.

There is little difference between $f(R)$ gravity and GR for the lensing tangential shear profile close to void centres. To distinguish between different models, it is more promising to use the shear signal at $0.7 r_{\text{void}} \lesssim r \lesssim 1.7 r_{\text{void}}$, where the tangential shear profiles may differ by 20-30%. Quantitatively, this is illustrated by the cumulative S/N shown on the right-hand panel of Fig. 14. The contribution for the S/N from $r < r_{\text{void}}$ is relatively minor. The S/Ns rise sharply at $r = r_{\text{void}}$; they peak at about $1.5 r_{\text{void}}$, reaching 4

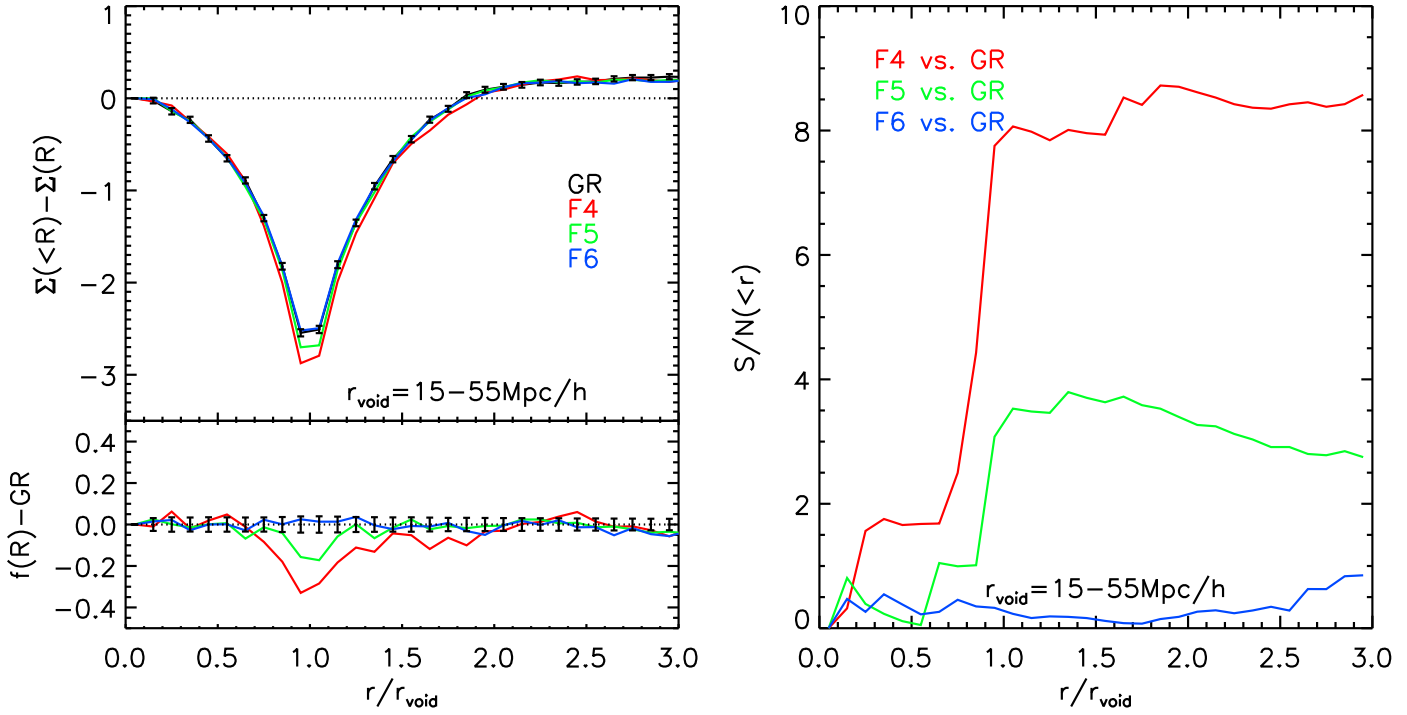


Figure 14. Left: like Fig. 12 but showing the lensing tangential shear profiles from stacking all voids with $15 < r < 55 \text{ Mpc}/h$. They are projected along two times void radius along the line of sight. $\Sigma(<R) - \Sigma(R)$ is proportional to the surface mass density within the projected radius of R subtracted by the surface mass density at R . Right: the corresponding cumulative (from small to large radius) S/N for the differences between GR and $f(R)$ models.

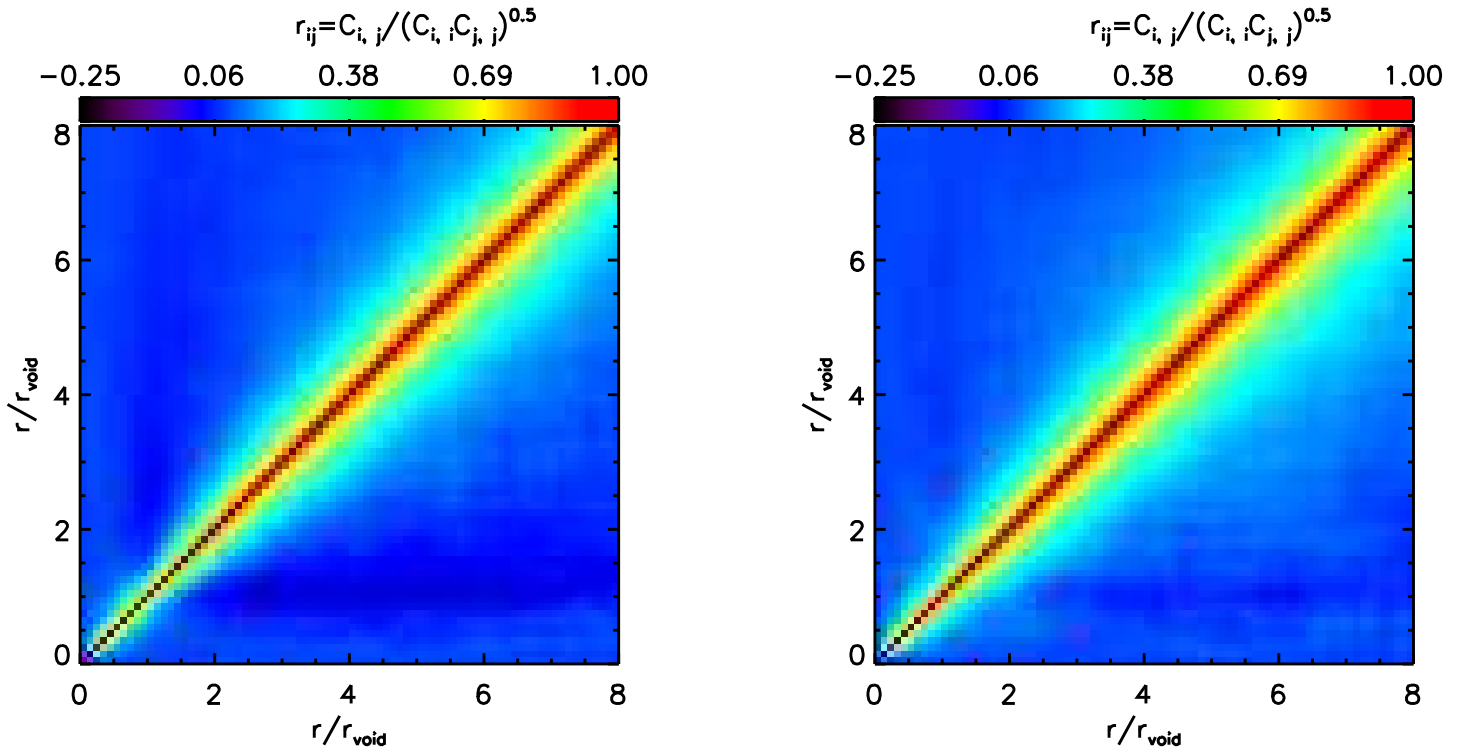


Figure 15. Covariance matrices of the predicted lensing tangential shear from stacking all voids with $15 < r < 55 \text{ Mpc}/h$ from the 1-Gpc/ h -a-side GR simulation. Left: the projection length along the line-of-sight is $2 \times r_{\text{void}}$; Right: the projection length is $8 \times r_{\text{void}}$.

and 8 respectively for F5 and F4. With the line-of-sight projection, F6 is not distinguishable from GR.

Note that the error bars given are just for the void sample from a volume of 1 (Gpc/h)^3 . Current BOSS DR11 CMASS sample has an effective volume of 6.0 (Gpc/h)^3 (Anderson et al. 2014; Beutler et al. 2013; Sánchez et al. 2014). In principle, the error bars shown in our figures should go down by a factor of 2.4 and the significance level should go up by the same factor if the BOSS DR11 CMASS sample is used. The future EUCLID survey (Laureijs et al. 2011) is expected to have an effective volume of $\sim 20 \text{ (Gpc/h)}^3$, a factor of 4.4 improvement is expected.

With our simulations, we explore the dependence of S/N for distinguishing $f(R)$ and GR models using the tangential shear signal on various aspects. Firstly, we find that including sub-voids are still useful to help increasing the S/N. With all sub-voids in our catalogue included, the number of voids increases by approximately 76%. This helps to increase the S/N to 7, and 12 for F5 and F4 respectively, but F6 still can not be told apart from GR, as its S/N does not get improved. Secondly, including voids with larger values of σ_4 (which means including voids that are potentially very different from spherical) also helps to increase the S/N, but very mildly. Finally, the projection of large-scale structure could bring extra noises or even bias the lensing signal associated with voids. To test this, we have integrated out to larger line-of-sight distances for the predicted tangential shear signal. Overall, we did not find the results to be biased when we integrated for more than twice the void radii, but the projection of large-scale structure introduced more noise and slightly larger covariances among the errors of different radial bins, as shown in Fig. 15. This make it harder to tell apart the different lines for different models, especially for large voids. Increasing the line-of-sight projection from 2 to 6 times of void radii decreases the S/N by about 30%.

The last point adds challenges for accurate measurement of the tangential shear profiles of voids. The density contrasts of voids are not as great as those of haloes. In other words, the amplitude of the shear signal associated with voids is relatively small, making it more vulnerable to noises such as that introduced by line-of-sight projection. This could set the upper bound for the power of constraining $|f_{R0}|$ using the tangential shear signal of voids. We have already seen this from the fact that F6 becomes indistinguishable from GR with the contamination of large-scale structure *in a 1 (Gpc/h)³ volume*.

Note that we have not included lensing shape noise for this study, since in general, shape noise may be subdominant compared to the noise from line-of-sight projection of large-scale structure for a DETF Stage IV type of deep imaging survey (Albrecht et al. 2006). Especially, the effect of shape noise is even less at relatively large radius of voids (Krause et al. 2013; Higuchi et al. 2013), which is the region of our interest to distinguish GR from $f(R)$ gravity. For a lensing survey covering 5000 deg^2 of the sky, with the number density of source galaxies being $n_{\text{gal}} = 12 \text{ arcmin}^{-2}$, the rms of the ellipticity distribution of galaxies $\sigma_\epsilon = 0.3$ and a mean redshift of ~ 1 , the lensing shape noise is clearly subdominant from the radius they show in Fig. 2, which is about $0.3 \times r_{\text{void}}$ (Krause et al. 2013). For a survey of similar settings, Higuchi et al. (2013) also find that lensing shape noise has little effect at large scales [See Table 4, Table 5 and Fig. 6 of Higuchi et al. (2013) for quantitative comparisons for the lensing S/N with or without shape noise.] Therefore, in the regime of $r > 0.7r_{\text{void}}$ where the shear profiles in $f(R)$ gravity differs from GR, it is relatively safe to ignore shape noise for deep imaging survey. At the very precise level, the importance of shape noise varies with the specific design of the

lensing survey as well as how it is combined with the (spectroscopic redshift) survey that are necessary to identify voids. For example, a deeper lensing survey with good image quality tend to have smaller shape noise per galaxy, hence the contribution to the noise covariance from lensing shape noise may be relatively minor. We leave it for future studies to figure out the contribution of shape noise for particular surveys.

To conclude this subsection, we caution that forecasts for the lensing measurement without including shape noise may be somewhat optimistic. In real observations, the significant levels may be degraded by the lensing shape noise, which is determined by the combination of the image quality of the source galaxies and the survey depth. Nevertheless, the first measurements of the lensing shear signal behind cosmic voids has been conducted using the SDSS data (Clampitt & Jain 2014). In their analysis, voids are found using LRGs. The tangential shear signals are measured for the stacked lensing source galaxies behind the stacked void center. A 13σ shear signal associated with the stacking of those voids has been found, which seems surprisingly better than expected from Krause et al. (2013).

5.3 Void velocity profiles

Velocities of dark matter, as the first integral of forces, should in principle react more sensitively to the differences among different gravity models than the density field. To investigate this, we present different components of velocity profiles for dark matter in Fig. 16 and for haloes in Fig. 17.

The radial velocity profiles, shown as solid curves, peak at $r \sim r_{\text{void}}$, consistent with the sharp rise in the density profiles. The sign of the radial velocity being positive means there is coherent outflow of mass. For relatively small voids ($r_{\text{void}} = 15 - 25 \text{ Mpc/h}$), the outflow is about 5, 15 and 35 km/s or $\sim 5\%$, 15% and 35% greater than GR for F6, F5 and F4 at $r \sim r_{\text{void}}$. Results for larger voids ($r_{\text{void}} = 35 - 55 \text{ Mpc/h}$) are shown on the right: they are qualitatively similar to those of smaller voids, except that the matter outflows are much stronger. It peaks at $r \sim r_{\text{void}}$ at about 300 km/s for GR, and for F4 it can be greater by nearly 60 km/s. Indeed, this level of difference is mildly greater than that in the density profiles shown in Fig. 12. The fact that the outflow velocity in $f(R)$ gravity is greater than in GR is also expected from the analytical work of Clampitt et al. (2013): in $f(R)$ gravity, the outward pointing fifth force from void centres drives dark matter to evacuate faster from the voids.

At $r > r_{\text{void}}$, the radial velocity profiles decrease farther away from the void centres. For small voids shown on the left, they turn negative at $r \sim 1.5r_{\text{void}}$, which means there is net inflow of mass. This is a clear signature of void-in-cloud. For large voids shown in the right-hand panel, the radial velocity profiles stay above zero, as expected for void-in-void, and the outflow of mass remains beyond $r \sim 3r_{\text{void}}$.

Fig. 16 also presents the mean tangential velocity as well as the radial and tangential velocity dispersions. It is interesting to see that all these components of velocities have similar levels of fractional differences between $f(R)$ models and GR. Fig. 17 presents the same results for haloes. All the above results regarding velocities in the dark matter field are confirmed using haloes, although the latter is noisier. We have also computed the velocity profiles for voids identified using GR void centres, and the results are shown in Fig. 18 in the Appendix; there is very little difference from Fig. 16, where the $f(R)$ and GR void centres are independent.

The velocity dispersion in $f(R)$ models being greater than in

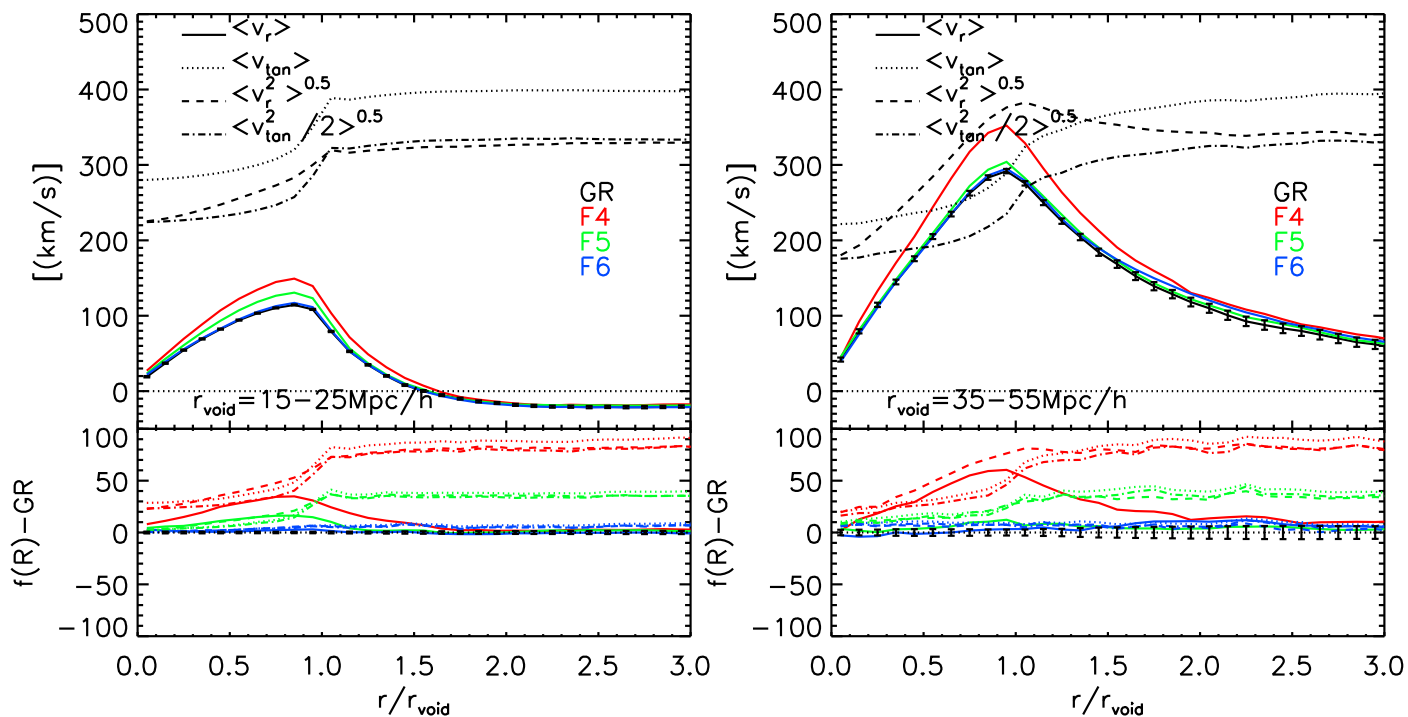


Figure 16. Top panels: different components of dark matter particle velocities with respect to the center of voids defined using haloes for simulations of different models labelled in different colours in the legend. Solid lines – the mean radial velocity profiles; dotted lines – the mean tangential velocity profile; dashed lines – the dispersion of the radial velocities; dash-dotted lines – the dispersion of half of the tangential velocities. For simplicity, for velocity profiles of $f(R)$ models, only the radial velocity profiles are plotted. One can appreciate their differences in respect to GR at the bottom panels. Error bars shown on the black line (GR) are the scatter about the mean for voids of $15 \text{ Mpc}/h < r_{\text{void}} < 25 \text{ Mpc}/h$ (left) and $35 \text{ Mpc}/h < r_{\text{void}} < 55 \text{ Mpc}/h$ (right) found within the $1 (\text{Gpc}/h)^3$ volume.

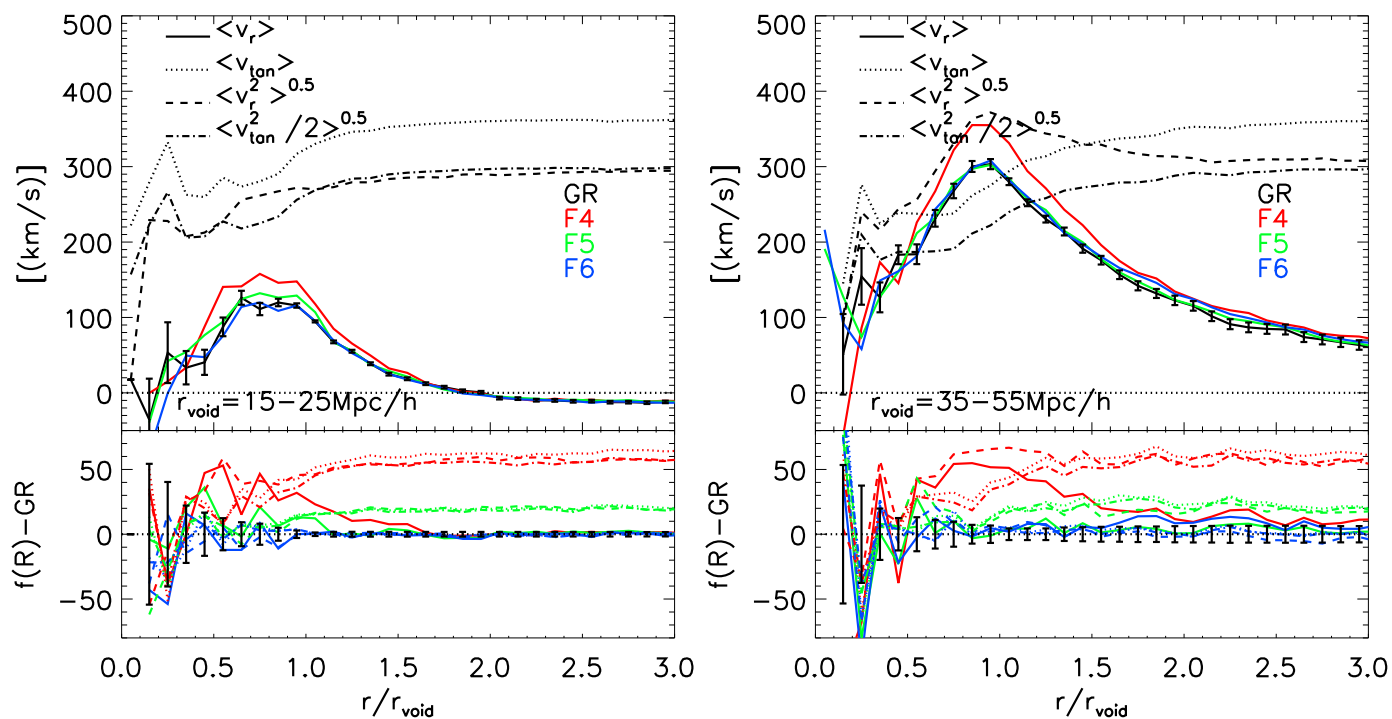


Figure 17. Similar to 16 but showing different components of velocity profiles traced by haloes.

GR provides another observable for testing $f(R)$ gravity. Stacking of galaxies around central galaxies in phase space has been proposed to measure the halo mass at a few times the virial radius, and has been applied by Lam et al. (2012) for testing gravity. The level of differences we have found for the velocity dispersion between $f(R)$ gravity and GR are $\sim 5\%$, 10% and 20% for F6, F5 and F4. These are consistent with what was found in Lam et al. (2012) for the case of stacked haloes in phase space for the same models (see Hellwing et al. 2014, for a test of modified gravity along the same line).

Before leaving this section, we note that differences between models in the velocity and density field can be best captured by the the clustering of voids in redshift space. We will conduct detailed studies of voids in redshift space in a separate paper.

6 CONCLUSION AND DISCUSSION

To briefly summarise, in this paper we have studied void properties in $f(R)$ gravity using N-body simulations of $f(R)$ (Hu & Sawicki 2007) and GR Λ CDM models of the same initial conditions and the same expansion history. In $f(R)$ models, the repulsive fifth force in voids drives them to grow larger and expand faster. This leads to a range of observables that are potentially powerful to distinguish $f(R)$ gravity from GR. In particular, we have found that:

- The void abundances in $f(R)$ gravity can differ significantly from in GR, if voids are identified using the dark matter field. More explicitly, the Hu-Sawicki $f(R)$ model with $f_{R0} = -10^{-4}$ (F4) shows a $\sim 100\% - 400\%$ enhancement of the void abundance over GR in the void radius range of $10 \sim 20$ Mpc/h; the enhancement in $f(R)$ models with $f_{R0} = -10^{-5}$ (F5) and $f_{R0} = -10^{-6}$ (F6) is smaller, but still at $\sim 70\% - 100\%$ and $\sim 20\%$, respectively, in the same radius range. However, if we (more realistically) identify voids using the dark matter haloes with the same space density, the difference from GR becomes much smaller, nearly disappearing at $r_{\text{void}} \lesssim 25$ Mpc/h, for all three variants of $f(R)$ gravity. This shows that void abundance alone is not an ideal observable to constrain $f(R)$ gravity.

- We find the counter-intuitive result that, if voids are identified in the halo field, then $f(R)$ gravity produces fewer large voids ($r_{\text{void}} \geq 30$ Mpc/h) than in GR. This is because, thanks to the fifth force, haloes are more likely to form in under-dense regions in the $f(R)$ model, which makes low density regions in this model less empty of halos even though they are emptier of dark matter. For the same void regions, $f(R)$ models are less empty of haloes (Fig. 9), but they are indeed emptier in terms of total dark matter. This suggests that $f(R)$ gravity (or other modified gravities of the similar type) is unlikely be able to resolve the Local Void problem. There are observations suggesting that the Local Void (within the radius of 1-8 Mpc from the center of the local group) seems too empty of galaxies, which may be a problem for the Λ CDM model. (e.g. Peebles 2001; Tikhonov & Klypin 2009; Peebles & Nusser 2010), but see (Tinker & Conroy 2009; Xie et al. 2014) for different views. There are speculations that a different model with more rapid emptying of voids and piling up of matter on its outskirts may help to resolve the tension (Peebles & Nusser 2010). At face, it seems $f(R)$ model is one of such models that has the required feature, as we have seen that the dark matter profiles in $f(R)$ are emptier and the void ridges are sharper. However, the more rapid halo formation in void regions in $f(R)$ models will perhaps makes voids less empty of haloes. which is just the opposite to what is needed to resolve the tension.

- We find that the halo number density profiles of voids in $f(R)$ are not distinguishable from those of GR. However, the dark matter density profiles associated with these voids are emptier of dark matter in $f(R)$ models than in GR; their over-density ridges, if any, are more prominent than those in GR. The latter result agrees with previous results based on the spherical expansion model of voids (Clampitt et al. 2013), which predicts that voids in $f(R)$ gravity are emptier and larger. Our results ring the alarm that void profiles can be very different depending on whether we are considering halo number or dark matter density profiles. This is not surprising from our prospective. Haloes or galaxies are biased tracers of the underlying dark matter density field. With relatively massive haloes whose linear bias is greater than unity, we do see the profiles of voids measured using haloes to be steeper than that of dark matter. This is essentially due to the fact that the amplitudes of the large-scale clustering of haloes are greater than those of dark matter. Note that this is different from the conclusion in (Sutter et al. 2014) that identical radial density profiles between galaxies and dark matter are recovered, though they have used a different void finder. i.e. ZOBOV.

- Two different types of voids, void-in-cloud and void-in-void are clearly seen in either halo number density profiles or dark matter profiles, the former having sharp over dense ridges but not for the latter. This is consistent with the radial velocity profiles, which indicates a regime of mass inflow for void-in-clouds, but not for void-in-voids. This is consistent with what has been found using ZOBOV for dark matter from simulations (Hamaus et al. 2014). For this reason, we argue that in principle it is not possible to find a universal void profile with a single rescaling parameter, i.e. the void radius. A second parameter to characterize the height of the overdense ridge is necessary. Note that this is different from Nadathur et al. (2014) who find that voids in their simulated LRG catalogues are self-similar, but they have used ZOBOV as their void finder for mock and real LRGs, and applied further selections on their voids. Also, it should be noticed that the sizes of voids studied by Nadathur et al. (2014) are on the large size end of the void size spectrum. These are usually of the void-in-void type according to our results and can indeed be described by a radius scaling alone. We find that only smaller voids show a ridge and can be described as void-in-clouds. For them to be described by a density profile formula an extra parameter is needed (e.g. Paz et al. 2014).

- The dark matter density profiles of voids can be measured using weak gravitational lensing. Observationally, this requires the combination of a galaxy redshift survey and a weak lensing survey over the same area of the sky. The idea of overlapping sky surveys has been promoted by the combination of redshift space distortion with lensing, which is another powerful way of constraining the linear growth hence gravity (Bernstein & Cai 2011; Cai & Bernstein 2012; Gaztañaga et al. 2012; de Putter et al. 2013; Kirk et al. 2013). With this setting of surveys, voids will be identified using tracers like galaxies/haloes from the redshift survey. The shear signal of the background galaxies (from the deeper lensing survey) associated with the voids will be stacked around the void centres. We demonstrate that the lensing tangential shear profiles can be used to constrain $f(R)$ gravity. For a survey volume of about $1 (\text{Gpc}/h)^3$, GR can be distinguished from F5 and F4 by 4 and 8σ respectively. Most of the signal comes the edge of the voids where the density profiles are the steepest. The S/N is lower for larger voids as their abundance is much smaller and profiles less steep. We stress that the estimates of S/N are somewhat optimistic since we do not account for lensing shape noise and other systematics. Note that the S/N can be improved by a few times by employing

the current BOSS survey or future EUCLID survey. We also found that including sub-voids is useful for increasing the S/N. Line-of-sight projection of large-scale structure degrades the S/N among models and may set limits on the constraint of $|f_{R0}|$. We find that F6 is not distinguishable from GR in terms of lensing of voids for this reason.

- Model differences in the velocity profiles are slightly greater than in the density profiles. This offers a good opportunity to constrain $f(R)$ gravity by studying voids in redshift space. This is particularly true for F4, which shows the strongest deviation from GR, while the constraints on F5 and F6 will be relatively weaker. A detailed study will be presented in a forthcoming paper.

We caution that our study of void properties are based on using haloes as tracers. In principle, haloes are accessible through the observations of galaxy clusters and groups. Compared with galaxies, this observable suffers from the sparseness of samples and the relatively large uncertainties in determining the halo mass. Therefore, it may seem that galaxies are more direct observables to probe voids. However, the complexity of galaxy formation physics, which is likely to be different in $f(R)$ gravity from GR in a non-trivial manner, will make the definition of voids in different models even more complicated and the results less reliable. In contrast, haloes can be found observationally in different ways, such as using lensing, X-ray clusters and Sunyaev-Zel'dovich effects, which are less affected by the galaxy formation physics. Furthermore, most of our results concern only the number density of haloes rather than their masses, and so are less affected by the uncertainties caused by halo mass measurements (which can be worse in $f(R)$ gravity because haloes can have different dynamical and lensing masses, depending on their masses and environments).

Recently, there has been rapidly growing interest in using cosmic voids to study cosmology or constrain gravity and dark energy models. In the two most well-studied categories of alternative gravity theories, the chameleon and Vainshtein types, the modification to GR is strongest in low-density regions, making voids a promising tool to constrain them. In this paper, we have demonstrated for a specific example that this is indeed true. Voids as a probe for cosmology has until very recently been considered as degraded by the ambiguities in the void definitions and void-finding algorithms. For example, Colberg et al. (2005) showed that different void finders do not agree even on the void abundances. Also, even applied on the same data set, different void-finding algorithms can output very different void density profiles (see, for examples, Pan et al. 2011; Nadathur et al. 2014, where the latter group, using the tessellation code ZOBOV, obtained significantly shallower void density profiles than what the former group found using a spherical under-density algorithm). However, as a void-finding algorithm is only a way to measure and quantify the distribution of dark matter, or its tracers such as galaxies and galaxy clusters, the detail of the algorithm itself is less relevant as long as one uses the same algorithm to find voids in the mock universe (i.e., simulations) and the real one.

Indeed, although often considered as a disadvantage, the ambiguity of defining and identifying voids can also have positive consequences: even if one void-finding algorithm is not sensitive to the modifications of gravity, others may well be, and by trying different algorithms one can hopefully find the optimal one to constrain a given type of gravity theory. For example, when determining the radius of a void, we have tried two different methods: (1) we divide particles around prospective void centres into a number of bins, find the bin at which the accumulative density first exceeds Δ_{void} , and let the void radius equal the radius of this bin; (2) we do not do the binning, but instead calculate the accumulative density every time

when the void finder encounters another particle (or tracer), stopping when it first exceeds Δ_{void} , and taking the void radius as the distance between that particle and the void centre. Because of the sparseness of tracers in empty regions, we have found that the two methods can lead to different halo number density profiles, though the significant levels of deviation from GR and the dark matter density profiles (hence lensing signals) are stable. We will leave the study and comparison with other void-finding algorithms to future work.

Our results above have important implications for cosmological tests of gravity. It is often believed that cosmology can only place loose constraints on chameleon-type modified gravity theories, such as $f(R)$ gravity (see, for example, Lombriser 2014, for a recent review). Here, we see that the stacking of void profiles and tangential shears can put constraints almost as strong as those from astrophysical tests, which suffer from bigger uncertainties. As such, it points out a new powerful probe which can potentially be applied to other types of gravity theories as well.

ACKNOWLEDGMENTS

We thank Jiaxin Han, Marius Cautun, Shaun Cole, Carlos Frenk, Simon White, Rien van de Weygaert, Sergei Shandarin and John Peacock for helpful discussions and comments. YC is supported by the Durham Junior Research Fellowship. NP acknowledges support by Fondecyt Regular No. 1110328 and BASAL PFB-06 CATA. BL is supported by the Royal Astronomical Society and Durham University. YC and BL also acknowledge a grant with the RCUK reference ST/F001166/1.

The simulations and part of data analysis for this paper were performed using the DiRAC Data Centric system at Durham University, operated by the Institute for Computational Cosmology on behalf of the STFC DiRAC HPC Facility (<http://www.dirac.ac.uk>). This equipment was funded by BIS National E-infrastructure capital grant ST/K00042X/1, STFC capital grant ST/H008519/1, and STFC DiRAC Operations grant ST/K003267/1 and Durham University. DiRAC is part of the National E-Infrastructure. Part of the analysis was done on the Geryon cluster at the Centre for Astro-Engineering UC, which received recent funding from QUIMAL 130008 and Fondecyt AIC-57. Access to the simulations used in this paper can be obtained from the authors.

REFERENCES

- Achitouv I., Neyrinck M., Paranjape A., 2013, ArXiv e-prints
- Albrecht A., Bernstein G., Cahn R., Freedman W. L., Hewitt J., Hu W., Huth J., Kamionkowski M., Kolb E. W., Knox L., Mather J. C., Staggs S., Suntzeff N. B., 2006, ArXiv Astrophysics e-prints
- Amendola L., Frieman J. A., Waga I., 1999, MNRAS, 309, 465
- Anderson L., Aubourg É., Bailey S., Beutler F., Bhardwaj V., Blanton M., Bolton A. S., Brinkmann J., et al. 2014, MNRAS, 441, 24
- Bernstein G. M., Cai Y.-C., 2011, MNRAS, 416, 3009
- Beutler F., Saito S., Seo H.-J., Brinkmann J., Dawson K. S., Eisenstein D. J., Font-Ribera A., Ho S., et al. 2013, ArXiv e-prints
- Bos E. G., van de Weygaert R., Dolag K., Pettorino V., 2012, MNRAS, 426, 440
- Bos E. G. P., van de Weygaert R., Dolag K., Pettorino V., 2012, MNRAS, 426, 440

- Brax P., van de Bruck C., Davis A.-C., Shaw D. J., 2008, *Phys. Rev.*, D78, 104021
- Brookfield A. W., van de Bruck C., Hall L. M., 2006, *Phys. Rev.*, D74, 064028
- Cai Y.-C., Bernstein G., 2012, *MNRAS*, 422, 1045
- Cai Y.-C., Li B., Cole S., Frenk C. S., Neyrinck M., 2014, *MNRAS*, 439, 2978
- Cai Y.-C., Neyrinck M. C., Szapudi I., Cole S., Frenk C. S., 2013, *ApJ*, 786, 110
- Carroll S. M., De Felice A., Duvvuri V., Easson D. A., Trodden M., et al., 2005, *Phys. Rev.*, D71, 063513
- Ceccarelli L., Paz D., Lares M., Padilla N., Lambas D. G., 2013, *MNRAS*, 434, 1435
- Clampitt J., Cai Y.-C., Li B., 2013, *MNRAS*, 431, 749
- Clampitt J., Jain B., 2014, *ArXiv e-prints*
- Colberg J. M., Pearce F., Foster C., Platen E., Brunino R., Neyrinck M., Basilakos S., Fairall A., et al. 2008, *MNRAS*, 387, 933
- Colberg J. M., Sheth R. K., Diaferio A., Gao L., Yoshida N., 2005, *MNRAS*, 360, 216
- De Felice A., Tsujikawa S., 2010, *Living Rev.Rel.*, 13, 3
- de Putter R., Doré O., Takada M., 2013, *ArXiv e-prints*
- Gaztañaga E., Eriksen M., Crocce M., Castander F. J., Fosalba P., Marti P., Miquel R., Cabré A., 2012, *MNRAS*, 422, 2904
- Granett B. R., Neyrinck M. C., Szapudi I., 2008, *ApJ*, 683, L99
- Hamaus N., Sutter P. M., Wandelt B. D., 2014, *ArXiv e-prints*
- Hellwing W. A., Barreira A., Frenk C. S., Li B., Cole S., 2014, *Phys. Rev. Lett.*, 112, 221102
- Higuchi Y., Oguri M., Hamana T., 2013, *MNRAS*, 432, 1021
- Hotchkiss S., Nadathur S., Gottlöber S., Iliev I. T., Knebe A., Watson W. A., Yepes G., 2014, *ArXiv e-prints*
- Hu W., Sawicki I., 2007, *Phys. Rev. D*, 76, 064004
- Hu W., Sawicki I., 2007, *Phys. Rev.*, D76, 064004
- Ilić S., Langer M., Douspis M., 2013, *A&A*, 556, A51
- Jennings E., Baugh C. M., Li B., Zhao G.-B., Koyama K., 2012, *MNRAS*, 425, 2128
- Jennings E., Li Y., Hu W., 2013, *MNRAS*, 434, 2167
- Khoury J., Weltman A., 2004, *Phys. Rev.Lett.*, 93, 171104
- Kirk D., Lahav O., Bridle S., Jouvel S., Abdalla F. B., Frieman J. A., 2013, *ArXiv e-prints*
- Knollmann S. R., Knebe A., 2009, *ApJ*, 182, 608
- Krause E., Chang T.-C., Doré O., Umetsu K., 2013, *ApJ*, 762, L20
- Lam T. Y., Clampitt J., Cai Y.-C., Li B., 2014
- Lam T. Y., Nishimichi T., Schmidt F., Takada M., 2012, *Physical Review Letters*, 109, 051301
- Laureijs R., Amiaux J., Arduini S., Augeres J.-L., Brinchmann J., Cole R., Cropper M., Dabin C., et al. 2011
- Lavaux G., Wandelt B. D., 2012, *ApJ*, 754, 109
- Li B., 2011, *MNRAS*, 411, 2615
- Li B., Barrow J. D., 2007, *Phys. Rev.*, D75, 084010
- Li B., Barrow J. D., 2011, *Phys. Rev.*, D83, 024007
- Li B., Efstathiou G., 2012, *MNRAS*, 421, 1431
- Li B., Hellwing W. A., Koyama K., Zhao G.-B., Jennings E., Baugh C. M., 2013, *MNRAS*, 428, 743
- Li B., Zhao G., Teyssier R., Koyama K., 2012, *J. Cosmo. Astropart. Phys.*, 01, 051
- Li B., Zhao G.-B., Koyama K., 2012, *MNRAS*, 421, 3481
- Li B., Zhao H., 2009, *Phys. Rev.*, D80, 044027
- Llinares C., Mota D. F., Winther H. A., 2013
- Lombriser L., 2014
- Martino M. C., Sheth R. K., 2009, *ArXiv e-prints*
- Melchior P., Sutter P. M., Sheldon E. S., Krause E., Wandelt B. D., 2014, *MNRAS*, 440, 2922
- Nadathur S., Hotchkiss S., Diego J. M., Iliev I. T., Gottlöber S., Watson W. A., Yepes G., 2014, *ArXiv e-prints*
- Navarro I., Van Acoleyen K., 2007, *JCAP*, 0702, 022
- Neyrinck M. C., Gnedin N. Y., Hamilton A. J. S., 2005, *MNRAS*, 356, 1222
- Oyaizu H., 2008, *Phys. Rev.*, D78, 123523
- Padilla N. D., Ceccarelli L., Lambas D., 2005, *MNRAS*, 363, 977
- Padmanabhan N., Xu X., Eisenstein D. J., Scalzo R., Cuista A. J., Mehta K. T., Kazin E., 2012, *MNRAS*, 427, 2132
- Pan D. C., Vogeley M. S., Hoyle F., Choi Y. Y., Park C., 2011, *MNRAS*, 421, 926
- Paranjape A., Lam T. Y., Sheth R. K., 2011, *MNRAS*, 420, 1648
- Peebles P. J. E., 2001, *ApJ*, 557, 495
- Peebles P. J. E., Nusser A., 2010, *Nature*, 465, 565
- Planck Collaboration Ade P. A. R., Aghanim N., Armitage-Caplan C., Arnaud M., Ashdown M., Atrio-Barandela F., Aumont J., Baccigalupi C., Banday A. J., et al. 2013, *ArXiv e-prints*
- Puchwein E., Baldi M., Springel V., 2013
- Ricciardelli E., Quilis V., Varela J., 2014, *MNRAS*, 440, 601
- Sánchez A. G., Montesano F., Kazin E. A., Aubourg E., Beutler F., Brinkmann J., Brownstein J. R., Cuesta A. J., Dawson K. S., Eisenstein D. J., Ho S., et al. 2014, *MNRAS*, 440, 2692
- Schmidt F., Vikhlinin A., Hu W., 2009, *Phys. Rev.*, D80, 083505
- Sheth R. K., van de Weygaert R., 2004, *MNRAS*, 350, 517
- Sotiriou T. P., Faraoni V., 2010, *Rev.Mod.Phys.*, 82, 451
- Sutter P. M., Carlesi E., Wandelt B. D., Knebe A., 2014, *ArXiv e-prints*
- Sutter P. M., Lavaux G., Wandelt B. D., Weinberg D. H., Warren M. S., 2014, *MNRAS*, 438, 3177
- Sutter P. M., Pisani A., Wandelt B. D., 2014, *ArXiv e-prints*
- Teyssier R., 2002, *Astron.Astrophys.*, 385, 337
- Tikhonov A. V., Klypin A., 2009, *MNRAS*, 395, 1915
- Tinker J. L., Conroy C., 2009, *ApJ*, 691, 633
- Vainshtein A. I., 1972, *Physics Letters B*, 39, 393
- Xie L., Gao L., Guo Q., 2014, *MNRAS*, 441, 933
- Zhao G., Li B., Koyama K., 2011, *Phys. Rev.*, D83, 044007

7 APPENDIX

This appendix contains the plot showing the enhancements in dark matter velocities due to the fifth force, using common void centres as found from the GR simulation. This should be read in the context of the discussion in the main paper.

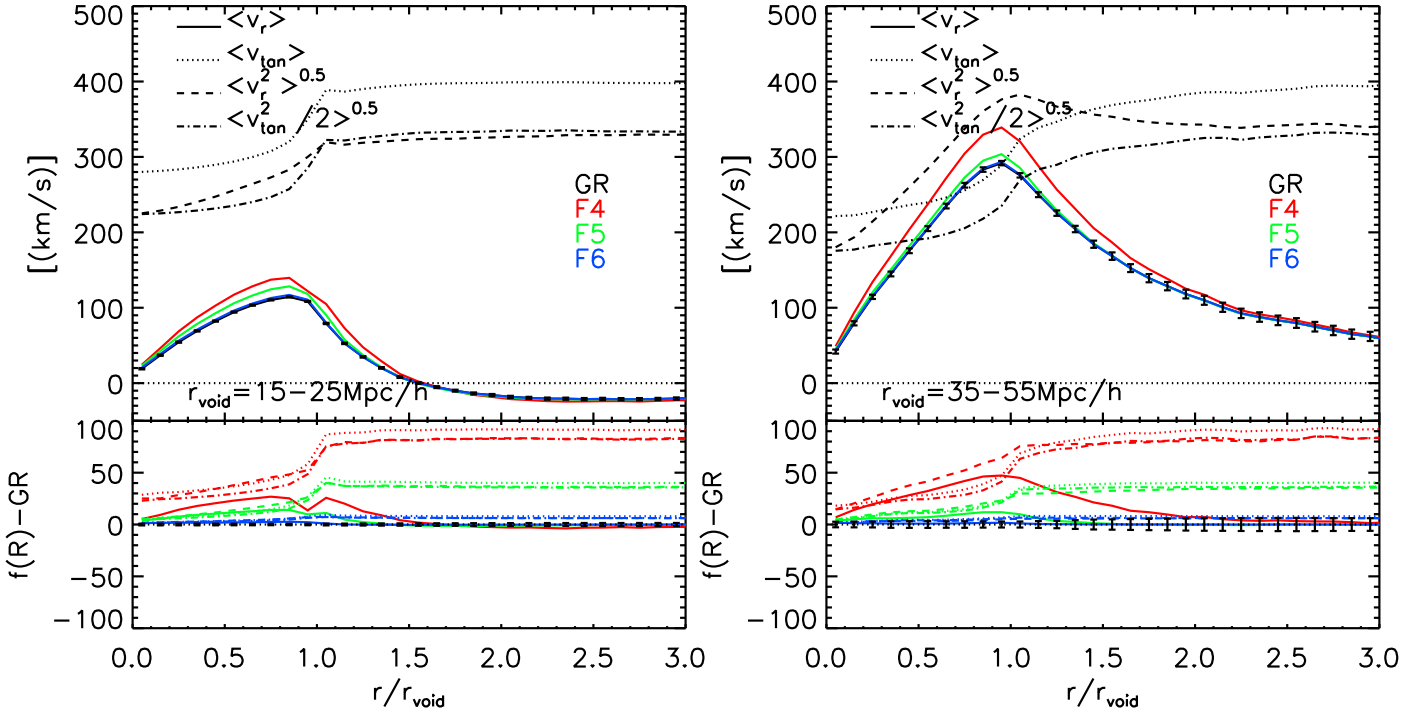


Figure 18. The same as Fig. 16, but showing results from using GR void centres to measure the profiles for all models. Top panels: different components of dark matter particle velocities with respect to the centre of voids defined using haloes for simulations of different models labelled in different colours in the legend. Solid lines – the mean radial velocity profiles; dotted lines – the mean tangential velocity profile; dashed lines – the dispersion of the radial velocities; dash-dotted lines – the dispersion of half of the tangential velocities. For simplicity, for velocity profiles of $f(R)$ models, only the radial velocity profiles are plotted (coloured solid lines). Their absolute differences with respect to GR are shown in the bottom panels. Error bars shown on the black line (GR) are the scatter about the mean for voids with $15 \text{ Mpc}/h < r_{\text{void}} < 25 \text{ Mpc}/h$ (left) and $35 \text{ Mpc}/h < r_{\text{void}} < 55 \text{ Mpc}/h$ (right) found in the $1 (\text{Gpc}/h)^3$ simulation volume.